



HAL
open science

Insights on designing non-PGM catalyst layers at low humidity

Yongwook Kim, Luis Urbina, Tristan Asset, Marc Secanell, Plamen Atanassov, Jake Barralet, Jeff Gostick

► **To cite this version:**

Yongwook Kim, Luis Urbina, Tristan Asset, Marc Secanell, Plamen Atanassov, et al.. Insights on designing non-PGM catalyst layers at low humidity. *Journal of Power Sources*, 2023, 562, pp.232741. 10.1016/j.jpowsour.2023.232741 . hal-04296082

HAL Id: hal-04296082

<https://hal.science/hal-04296082>

Submitted on 20 Nov 2023

HAL is a multi-disciplinary open access archive for the deposit and dissemination of scientific research documents, whether they are published or not. The documents may come from teaching and research institutions in France or abroad, or from public or private research centers.

L'archive ouverte pluridisciplinaire **HAL**, est destinée au dépôt et à la diffusion de documents scientifiques de niveau recherche, publiés ou non, émanant des établissements d'enseignement et de recherche français ou étrangers, des laboratoires publics ou privés.

Insights on Designing non-PGM Catalyst Layers at Low Humidity

Yongwook Kim¹, Luis P. Urbina², Tristan Asset^{3,4}, Marc Secanell², Plamen Atanassov⁴, Jake Barralet⁵,
Jeff T. Gostick^{1,*}

¹Department of Chemical Engineering, University of Waterloo, Waterloo, ON N2L 3G1, Canada

²Department of Mechanical Engineering, University of Alberta, Edmonton, AB T6G 2R3, Canada

³Institute of Chemistry and Processes for Energy, Environment and Health (ICPEES), UMR 7515
CNRS-Université de Strasbourg, 25 rue Becquerel, 67087 Strasbourg Cedex 02, France

⁴Department of Chemical and Biomolecular Engineering, University of California, Irvine, CA 92697,
United States

⁵Faculty of Dentistry, McGill University, Montreal, QC H3A 0C7, Canada

*Corresponding Author: jgostick@uwaterloo.ca

Keywords

Precious group metal-free catalyst; Sacrificial support method; Catalyst layer; PEM Fuel Cell; Finite elements

Abstract

Non-precious group metal (non-PGM) catalysts offer the opportunity to significantly reduce fuel cell costs. However, owing to its low volumetric activity, non-PGM electrodes are made an order of magnitude thicker than platinum-based electrodes. Thicker electrodes increase transport losses making it critical to optimize electrode composition. In most studies, non-PGM electrodes are tested with fully humidified O₂ /air to maximize the proton conductivity. However, the fully humidified inlet gas makes non-PGM electrodes more prone to water flooding which can cause long-term performance degradation. In the present study, a single-phase, non-isothermal model was used to investigate the structure-performance relationships of the non-PGM electrodes operated at low relative humidity. Our modeling study reveals that high porosity is not necessarily required for non-PGM electrodes operating at low relative humidity. Instead, high solid and electrolyte phase volume fractions are desired. Our proposed strategy is to reduce the thickness of the non-PGM electrode while keeping the mass loading of the non-PGM catalyst consistent.

1. Introduction

One of the major bottlenecks for wider adoption of polymer electrolyte membrane fuel cells (PEMFCs) is the use of expensive platinum catalysts [1,2]. There have been many efforts to reduce the amount of platinum catalysts [3–9]. However, platinum is projected to be responsible for approximately 40% of the total PEMFC stack cost even at an optimistic loading (e.g., $0.125 \text{ mg}_{\text{Pt}} \text{ cm}^{-2}$) [10]. An ideal solution to lowering stack cost is to replace the platinum with non-precious group metal (non-PGM) catalysts. A recent cost analysis of PEMFC technology shows that replacing platinum with non-PGM catalysts can save $\text{US}\$6 \text{ kW}^{-1}$ from the total stack cost, which is a significant milestone toward meeting the ultimate target of $\text{US}\$30 \text{ kW}^{-1}$ set out by the US Department of Energy (US DOE) [11].

Among different types of non-PGM catalysts, transition metal-based (e.g., M-N-C with M = Fe, Co, Mn) catalysts have shown the most promise over the past years [12–18]. Unfortunately, the intrinsic activity of the non-PGM catalysts is still low compared to the platinum-based catalysts. A modeling study suggests that the active site density (e.g., M-N_x) needs to increase by at least 40 times for the non-PGM catalysts to meet the performance target proposed by the US DOE [19]. However, with such high metal content (e.g., >5 wt.%), the metal atoms aggregate to form metal particles during pyrolysis steps which leads to even lower intrinsic activity [20]. Therefore, a more effective, short term approach for improving the performance of non-PGM catalyst layers is to maximize the utilization of the available catalytic sites by optimizing the catalyst layer structures and compositions [21–23]. The complication is that the non-PGM catalyst layers must be made an order of magnitude thicker than their platinum-based counterparts to compensate for the low volumetric activity. Thicker layers cause several challenges, such as increased transport resistances for oxygen, protons, and electrons. Structure and composition optimizations of the non-PGM catalyst layers offer the opportunity to increase the fuel cell performance by minimizing these

transport resistances.

Optimizing the catalyst layer structure and composition is not a straightforward task due to competing requirements for each of the transport processes occurring simultaneously within the membrane electrode assembly. In addition, a large number of design variables for the catalyst layers add complexity to the engineering of the non-PGM catalyst layers. Experimental studies up to date have looked at the effect of catalyst loading [24–26], ionomer loading [27–30], and ionomer equivalent weight [27] on the performance of the non-PGM electrodes. Also, there is an ongoing efforts to understand H^+ transport [28,29], gas diffusivity [31–33], and liquid water transport [34–36] in the thick non-PGM electrodes. However, most of these studies tested non-PGM electrodes with fully humidified O_2 /air. High relative humidity (RH) minimizes the proton transport resistance by increasing the proton conductivity of the ionomer, but it also leads to electrode flooding. Although, a short-term efficiency loss from excess liquid water is not a significant problem [37,38], it causes the long-term efficiency losses by channel flooding [39] and mechanical degradation of the membrane [40]. For these reasons, practical fuel cell operation regimes avoid formation of liquid water.

In the present study, we present and explore a potential strategy for improving the performance of the non-PGM electrodes by optimizing the non-PGM electrode structure under conditions of practical relevance (i.e., 70% RH inlet gas). We carried out the study using a continuum-based, single-phase, non-isothermal model in lieu of experimental optimization to moderate the complexity of the electrode design. We first calibrated the model with experimental polarization curves collected with non-PGM electrodes with different ionomer loadings by adjusting the reference exchange current density and the effective electrical conductivity. We used the calibrated model to investigate the structure/composition-performance relationships of the non-PGM electrodes by adjusting important properties of the non-PGM

catalyst layers (i.e., reference exchange current density, catalyst loading, and thickness).

Our study reveals that if the catalytic activity of the non-PGM catalyst improved to the level that of platinum, the non-PGM catalyst layer can achieve the performance targets proposed by various institutions (i.e., US DOE, ElectroCat) by simple tuning of the catalyst mass loading. This is because less catalyst can be used with more active non-PGM catalyst which leads to decreased transport resistances. Otherwise, if the activity of the non-PGM catalysts stays as they currently are, optimization of the structure and composition of the non-PGM catalyst layer must be considered. Our study also indicates that when the RH of the air inlet is low, high porosity is not required as suggested by other studies that were tested with 100% RH [23,27]. This is attributed to lower chance of electrode flooding at low RH, therefore high pore volume is not required to accommodate the higher water content.

2. Experimental

2.1. Fuel cell assembly and testing

Iron-nicarbazin (Fe-NCB) electrocatalysts were prepared by the sacrificial support method [41,42]. The non-PGM cathodes were electrosprayed onto Sigracet® SGL 25BC following a previously reported procedure [33]. The dry weight of the ionomer (Nafion® EW 1100) in the cathode was adjusted to be either 30, 50, or 70 wt.% of the total solid deposit. The catalyst inks were deposited until the catalyst loading was 3 mg cm^{-2} . The anode catalyst layer was fabricated by inkjet-printing on a Nafion® NRE-211 membrane using a Fujifilm printer (Dimatix DPM-2800) [3,4]. The anode's catalyst ink consisted of Pt/C catalyst (HySa-K40, 40 wt.% EC300J, HyPlat®), and Nafion® ionomer solution (Liquion 5 wt% LQ-1105, Ion Power) suspended in an isopropyl alcohol and propylene glycol solution. The anode's total platinum loading was fixed at 0.1 mg cm^{-2} with a 30 wt.% ionomer content. To assemble the membrane electrode assemblies (MEAs), the electrosprayed non-PGM gas diffusion electrodes were hot pressed to the membrane with the inkjet-printed anodes and a Sigracet® SGL 28BC gas diffusion layer (GDL). The electrodes were compressed at 110°C for 10 min under 450 psi. The GDL compression was controlled by PTFE-coated fiber glass gaskets with a thickness of $300 \mu\text{m}$ for the cathode, and $150 \mu\text{m}$ for the anode side to get an approximate $50 \mu\text{m}$ compression of the GDLs. To ensure a proper compression of the MEAs, a pressure sensor film (Fujifilm Prescale super-low LLW) was used during cell assembly.

PEMFC tests were performed with a Scribner 850e test station. The MEAs with a 5 cm^2 active area were fixed between graphite plates with a single serpentine channel. Before testing, each assembled sample was conditioned at 80°C and 1.5 atm pressure with fixed flow rates of 0.2 and 0.4 slpm of hydrogen, and air, respectively, at 80% RH. The current was slowly increased in steps from 0.1 A to the maximum current obtained by the cell before reaching 0.2 V. After conditioning, potentiostatic polarization plots

were recorded from open circuit voltage to 0.2 V at steps of 20 mV every 45 sec using a cell temperature of 80°C and 1.5 atm total pressure. The gas feed was fixed 0.2 and 0.6 slpm of hydrogen and air respectively at 50, 70, and 90% RH. At least two samples of each cathode's ionomer content were tested to check for reproducibility.

3. Model description

The membrane electrode assembly (MEA) was modeled as a simplified across-the-channel two-dimensional geometry (Figure 1a). The computational domain was treated as a continuum to describe the various transport processes occurring in the MEA (Figure 1b). Anode and cathode each consisted of a gas diffusion layer (GDL), a microporous layer (MPL) and a catalyst layer (CL). GDLs were modeled as anisotropic (caused by the orientation of the fibers) whereas the other layers were assumed to be isotropic. Both anode and cathode catalyst layers were assumed to be a homogeneous mixture of solid catalyst material, ionomer, and void space. Channels and lands were treated as boundary conditions. Dimensions are specified in Table B.1 in the Appendix.

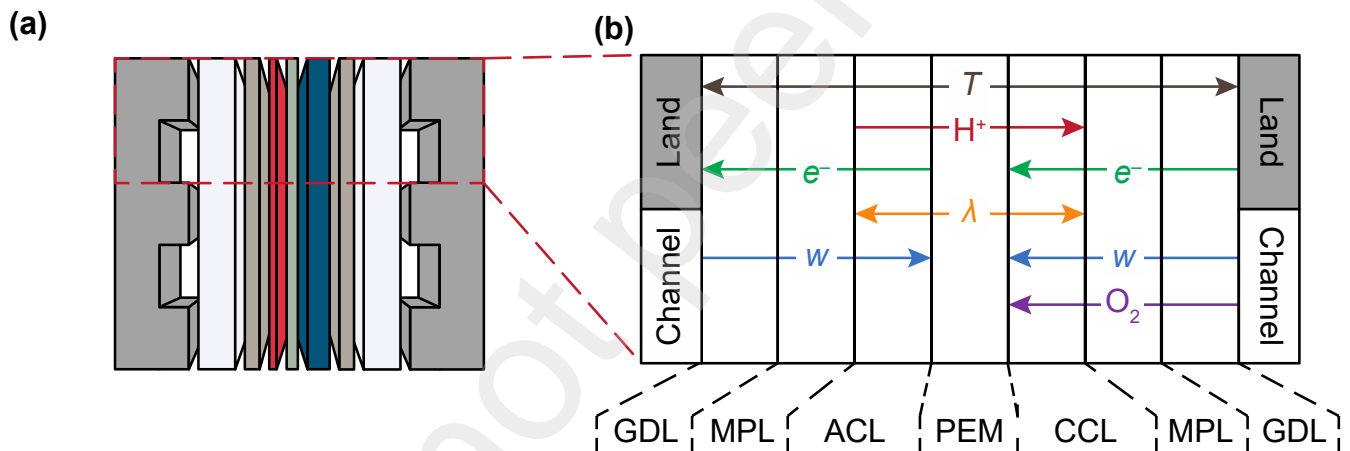


Figure 1 Schematics of (a) the modeled domain in a proton exchange membrane fuel cell assembly and (b) the modeled transport processes within the membrane electrode assembly. Across-the-channel, single-phase, non-isothermal model was used in this work. *Abbreviations*: gas diffusion layer (GDL); microporous layer (MPL); anode & cathode catalyst layers (ACL & CCL, respectively); proton exchange membrane (PEM); temperature (T); proton (H^+); electron (e^-); sorbed water in the ionomer phase (λ); water vapor (w); oxygen gas (O_2).

The scope of this work was to study the behavior of the non-PGM catalyst layers operated under practical operating conditions (e.g., 70% RH, $E_{cell} = 0.675$ V, air-fed). Liquid water is less likely to condense in porous layers at these conditions. We therefore determined that a single-phase, non-isothermal

model would suffice the purpose of this work. This assumption was checked after each simulation, and we confirmed that the local RH within the membrane electrode assembly did not exceed 100% in most cases. Instances where the local RH exceeded 100% have been clearly marked in the data presented in this study.

3.1. Governing equations

We adapted the steady-state, single-phase, isobaric, non-isothermal model developed by Bhaiya et al. [43]. The governing equations are:

$$-\nabla \cdot (c_{tot} D_{O_2, N_2}^{eff} \nabla x_{O_2}) = S_{O_2} \quad (1)$$

$$-\nabla \cdot (c_{tot} D_{H_2O, (N_2 \text{ or } H_2)}^{eff} \nabla x_w) = S_w \quad (2)$$

$$-\nabla \cdot (\sigma_l^{eff} \nabla \phi_l) = S_{H^+} \quad (3)$$

$$-\nabla \cdot (\sigma_s^{eff} \nabla \phi_s) = S_{e^-} \quad (4)$$

$$-\nabla \cdot \left(n_d \frac{\sigma_l^{eff}}{F} \nabla \phi_l + \frac{D_\lambda^{eff}}{V_m} \nabla \lambda + \frac{D_T^{eff}}{M_{H_2O}} \nabla T \right) = S_\lambda \quad (5)$$

$$-\nabla \cdot (k^{eff} \nabla T) + \sum (j_i \cdot \nabla \bar{H}_i) = S_T \quad (6)$$

We excluded the transport of H₂ from the system of equations. The H₂ mole fraction can be obtained by (1 - x_w) since x_w is solved for in both anode and cathode (Figure 1b) [44]. The thermodynamic potential was calculated by the Nernst equation [45]. The volumetric current density of the anodic reaction was described by the dual-pathway kinetics proposed by Wang et al. [46]. The volumetric current density of the cathodic reaction was assumed to follow the Tafel kinetics. Fick's law was used to model the transport of all gaseous species (eq. (1)&(2)). We assumed that both oxygen and water vapor are dilute species in

nitrogen at the cathode. The anode reactant is a binary mixture of hydrogen and water vapor. The charge transport was described by Ohm's law (eq. (3)&(4)). The proton flux is only allowed in the electrolyte phase (i.e., CLs, membrane) whereas the electron transport occurs only in the solid phase (i.e., GDLs, MPLs, CLs). The transport of sorbed water was solved in the CLs and the membrane. The electro-osmotic effect, back diffusion, and thermo-osmotic effect were considered for sorbed water transport (eq. (5)). The thermal transport was solved in all MEA components. In thermal transport, it was assumed that conduction and diffusion were the dominant transport mechanisms whereas convection contribution was relatively small [43]. The thermo-diffusion effect and heat generation due to viscous dissipation were neglected (eq. (6)).

3.2. Source terms and phase transitions

A summary of source terms is given in Table 1.

Table 1 A summary of source terms

Source terms	GDL & MPL	ACL	CCL	Membrane
S_{O_2}	0	0	$-S_f/2$	0
S_w	0	$-S_\lambda$	$S_f - S_\lambda$	0
S_{H^+}	0	j	$-j$	0
S_{e^-}	0	$-j$	j	0
S_λ	0	S_λ	S_λ	0
S_T	$S_{j,e}$	$S_r + S_{j,p} + S_{j,e} + S_s$	$S_r + S_{j,p} + S_{j,e} + S_v + S_s$	$S_{j,p}$

Faraday's law determines the rate of O_2 consumption and water production:

$$S_f = \frac{j}{2F} \quad (7)$$

Absorption and desorption of water vapor into and out of the electrolyte phase occurs at a finite rate over

a time span (rate constant, k_t) [47]. The sorption source term, S_λ is introduced to the continuity equations of λ and x_w to account for this ionomer-gas interfacial transport resistance:

$$S_\lambda = \frac{k_t}{V_m}(\lambda_{eq} - \lambda) \quad (8)$$

The heat dissipated by the electrochemical reaction is given by the sum of activation and Peltier effect [48]:

$$S_r = \begin{cases} -j\eta - S_f(Tf_{ORR}\Delta\bar{S}_{overall}), & \text{in ACL} \\ j\eta - S_f[T(1 - f_{HOR})\Delta\bar{S}_{overall}], & \text{in CCL} \end{cases} \quad (9)$$

For consistency with the single-phase assumption, an additional heat sink term corresponding to complete vaporization of liquid water produced at the cathode is included:

$$S_v = -S_f\bar{H}_{lv} \quad (10)$$

where \bar{H}_{lv} is the latent heat of vaporization.

Ionic and electric currents cause Joule heating which are described by Joule's law:

$$\begin{aligned} S_{j,p} &= \sigma_l^{eff}(\nabla\phi_l \cdot \nabla\phi_l) \\ S_{j,e} &= \sigma_s^{eff}(\nabla\phi_s \cdot \nabla\phi_s) \end{aligned} \quad (11)$$

Finally, the latent heat of absorption/desorption during phase transition of water vapor in the catalyst layers is described by:

$$S_s = S_\lambda\bar{H}_{sorp} \quad (12)$$

where \bar{H}_{sorp} is the molar enthalpy of sorption.

3.3. Model parameters, boundary conditions, and numerical implementation

Most input parameters are reported by Bhaiya et al. [43]. A few exceptions are the parameters related to the non-PGM cathode. For instance, we have previously reported a Bruggeman's exponent (i.e., μ in

$\tau = \varepsilon^{\mu}$) for the electrosprayed non-PGM cathodes [33] measured by a customized tool [49]. We also assumed a value for the reference exchange current density of the oxygen reduction reaction and the tortuosity of the effective electrical conductivity of the non-PGM catalyst. These assumptions were made due to the scarcity of the available data. Detailed model and input parameters are provided in the Appendix.

The boundary conditions are listed in Table 2. It is assumed that the solution is continuous on the interfaces between layers. The boundary conditions assume a zero-flux boundary condition for all state variables, except at the GDL and current collector interfaces where electrode potential is specified, and at the GDL and gas channel interfaces where the mole fractions of the reactants are given.

Table 2 Boundary conditions

Variable	AGDL Channel	AGDL Land	CGDL Channel	CGDL Land
x_{O_2}	zero flux	zero flux	$x_{O_2,c}^{\circ}$	zero flux
x_w	$x_{w,a}^{\circ}$	zero flux	$x_{w,c}^{\circ}$	zero flux
ϕ_m	zero flux	zero flux	zero flux	zero flux
ϕ_s	zero flux	0	zero flux	E_{cell}
λ	zero flux	zero flux	zero flux	zero flux
T	zero flux	T_{cell}	zero flux	T_{cell}

The model used in this study was based on the non-isothermal MEA model implemented in the open source fuel cell simulation tool, openFCST [50]. The model has been shown to be able to predict platinum-based fuel cells by Bhaiya et al. [43]. To solve the nonlinear governing equations, a Newton solver with an absolute residual tolerance of 10^{-8} was used where spatial discretization is achieved using second order Lagrange finite elements. The linear system of equations was solved using UMFPACK [51]. A transient version of this model, including local transport resistances, was recently validated via polarization curves, cell resistance, and impedance spectroscopy by Kosakian et al. [52].

4. Results and discussion

4.1. Model calibration and validation

Due to the lack of available data on Tafel kinetic parameters for non-PGM electrodes, we adjusted the reference exchange current density (i_0^{ref}) while fixing the other kinetic parameters such as the transfer coefficient ($\alpha = 1$) [53,54] and the reaction order ($\gamma = 1$) [53,54]. $i_0^{ref} = 6 \times 10^{-13} \text{ A cm}^{-2}$ gave the best fit at low current densities for all experimental data. As a comparison, i_0^{ref} is in the order of 10^{-9} to $10^{-8} \text{ A cm}^{-2}$ for platinum-based cathode catalyst layers [53–57]. Some of the recent studies on Fe-N-C electrocatalysts report i_0^{ref} in the order of $10^{-11} \text{ A cm}^{-2}$ and the fitted i_0^{ref} is considerably low in comparison [17,18]. The low kinetics of the Fe-N-C electrocatalyst used in this study is ascribed to the shelf-aging. Poor shelf-life of Fe-N-C catalysts is caused by the ex-situ degradation of the electrocatalyst between its preparation and the preparation of the catalytic layer. The ex-situ degradation decreases the intrinsic activity of the electrocatalyst through the transformation of the Fe-N_x active sites in clusters and nanoparticles. To this end, two other exchange current density were considered in addition to the fitted i_0^{ref} of $6 \times 10^{-13} \text{ A cm}^{-2}$: (i) $6 \times 10^{-11} \text{ A cm}^{-2}$, which is more representative of the current state of the Fe-N-C intrinsic activity; and (ii) $8.3 \times 10^{-9} \text{ A cm}^{-2}$ to represent a case where the Fe-N-C exhibits intrinsic activity in the same range as that of the Pt-based electrocatalysts. Notwithstanding, this study aims to explore the structure/composition-performance relationship rather than to report a high-performing non-PGM electrode.

Our initial numerical parametric study on the ionomer loading predicted that 70 wt.% was the optimal ionomer loading. The experiments showed, however, that the optimal ionomer loading was 50 wt.% (Figure 2a). The effective proton conductivity should not, in principle, decrease with increasing ionomer

loading. Therefore, we attributed the discrepancy between experimental and model polarization curves to the reduced effective electrical conductivity (σ_s^{eff}) at high ionomer loadings. At high ionomer loadings, the catalyst particles are likely to be disconnected by the excess ionomer. Since the ionomer is electrically insulating, the electrons would experience extra resistance due to increased tortuosity in the catalyst phase at high ionomer loading (Figure 3).

Table 3 summarizes σ_s^{eff} obtained by adjusting the solid phase tortuosity (i.e., μ_s in eq. (A.15)) to fit the experimental polarization curves. At 70 wt.% ionomer loading, σ_s^{eff} is two orders of magnitude lower than the other two values. This substantial difference in σ_s^{eff} implies that the electron transfer is hindered at the high ionomer loading as illustrated in Figure 3. It is also noteworthy to mention that the non-PGM electrodes have higher porosities compared to the optimal porosities for platinum-based electrodes (Table 3) [33,54]. The implication of the high porosities in non-PGM electrodes is that they are not likely to suffer from O₂ depletion at high current densities, which is usually the case with low porosity platinum electrodes. High porosity, however, lowers the solid and electrolyte phase volume fractions leading to higher charge transport overpotentials. This point is further discussed later in this section.

Once we calibrated our model to the experimental data with different ionomer loadings, we investigated whether the model could predict the polarization curves at different relative humidity (RH). Both experimental and model polarization curves shifted toward higher current density region with increasing RH (Figure 2b). However, the experiment showed lesser degree of shift in polarization curves with changing RH.

Table 3 Phase volume fractions of non-PGM electrodes with different ionomer contents. The table also includes solid phase network constants (μ_s) for the percolation equation and the effective electrical conductivity (σ_s^{eff}) used in the model to fit the experimental polarization curves

Ionomer loading (wt.%)	ε_v (-)	ε_s (-)	ε_l (-)	μ_s (-)	σ_s^{eff} (S cm ⁻¹)
30	0.807	0.129	0.064	2.38	0.115
50	0.721	0.129	0.150	2.13	0.232
70	0.521	0.129	0.350	3.40	0.007

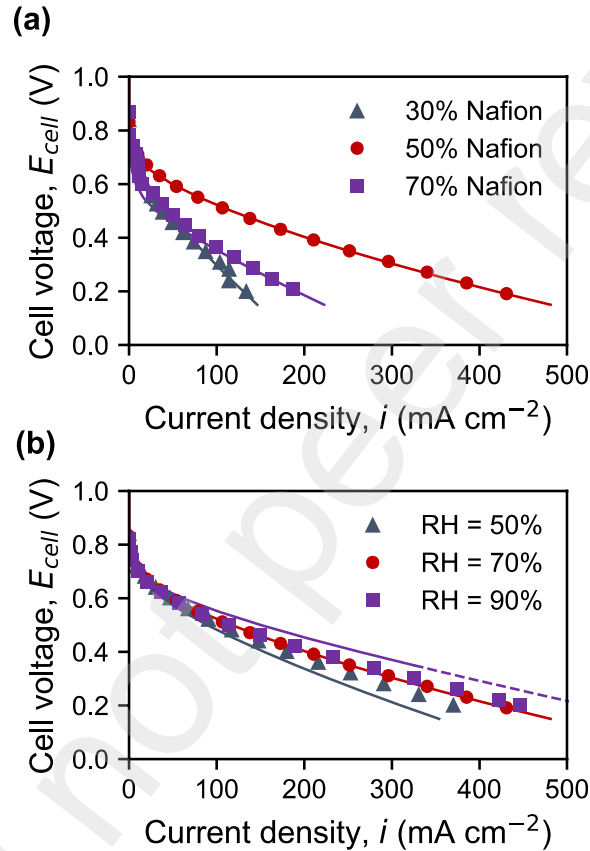


Figure 2 Model calibration and validation with experimentally measured polarization curves of 3 mg cm⁻² PGM-free electrodes with (a) 30, 50, and 70% ionomer content and PEMFC tested with 3 mg cm⁻² catalyst loading and 50% ionomer loading at (b) 50, 70, and 90% relative humidity. The markers represent the experimental data, and the solid lines represent simulated polarization curves. The dotted lines denote non-physical region where RH > 100%.

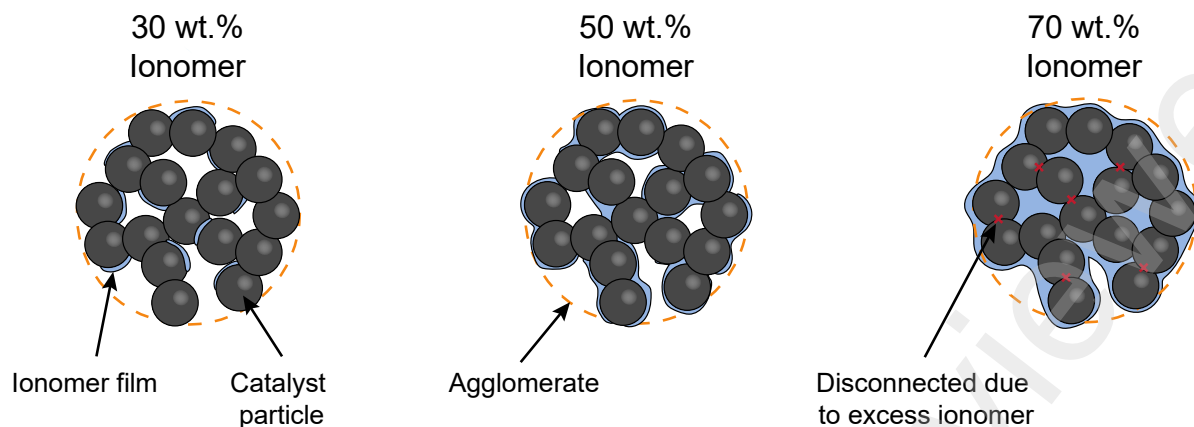


Figure 3 Illustration of ionomer coverage on non-PGM catalyst particles. At sufficient ionomer loading (i.e., < 50 wt%), ionomer covers the catalyst particles in thin film. However, at high ionomer loading (i.e., 70 wt.%), the ionomers can block percolating pathways for electrons. The reduced percolating pathways result in higher tortuosity for the electron transfer.

We plotted O_2 mole fraction, electrode potential, electrolyte potential, and the volumetric current density of the oxygen reduction reaction (ORR) of the non-PGM catalyst layers at $E_{cell} = 0.4$ V with different ionomer loadings to determine the limiting process for the non-PGM catalyst layer (Figure 4). A non-uniform O_2 concentration is observed inside the non-PGM electrodes. However, the concentration is sufficiently high everywhere and is not expected to affect the reaction adversely (Figure 4a). In contrast, the electrode and electrolyte overpotentials are high (Figure 4b&c). The high electrode and electrolyte overpotentials are caused by low phase volume fractions of the solid and electrolyte phases (Table 3). Consequently, a significant portion of the non-PGM layer is not utilized (Figure 4d). The ORR volumetric current density is close to zero everywhere except in a very narrow zone near either the membrane|cathode or cathode|MPL interface. Note, for non-PGM catalyst layer with 70 wt.% ionomer loading, the electrode overpotential is especially high due to high solid phase tortuosity. This leads to almost all non-PGM layer not being utilized (Figure 4d). Based on this analysis, we conclude that the performance of the non-PGM catalyst layer is mainly limited by the charged transport (i.e., e^- and H^+).

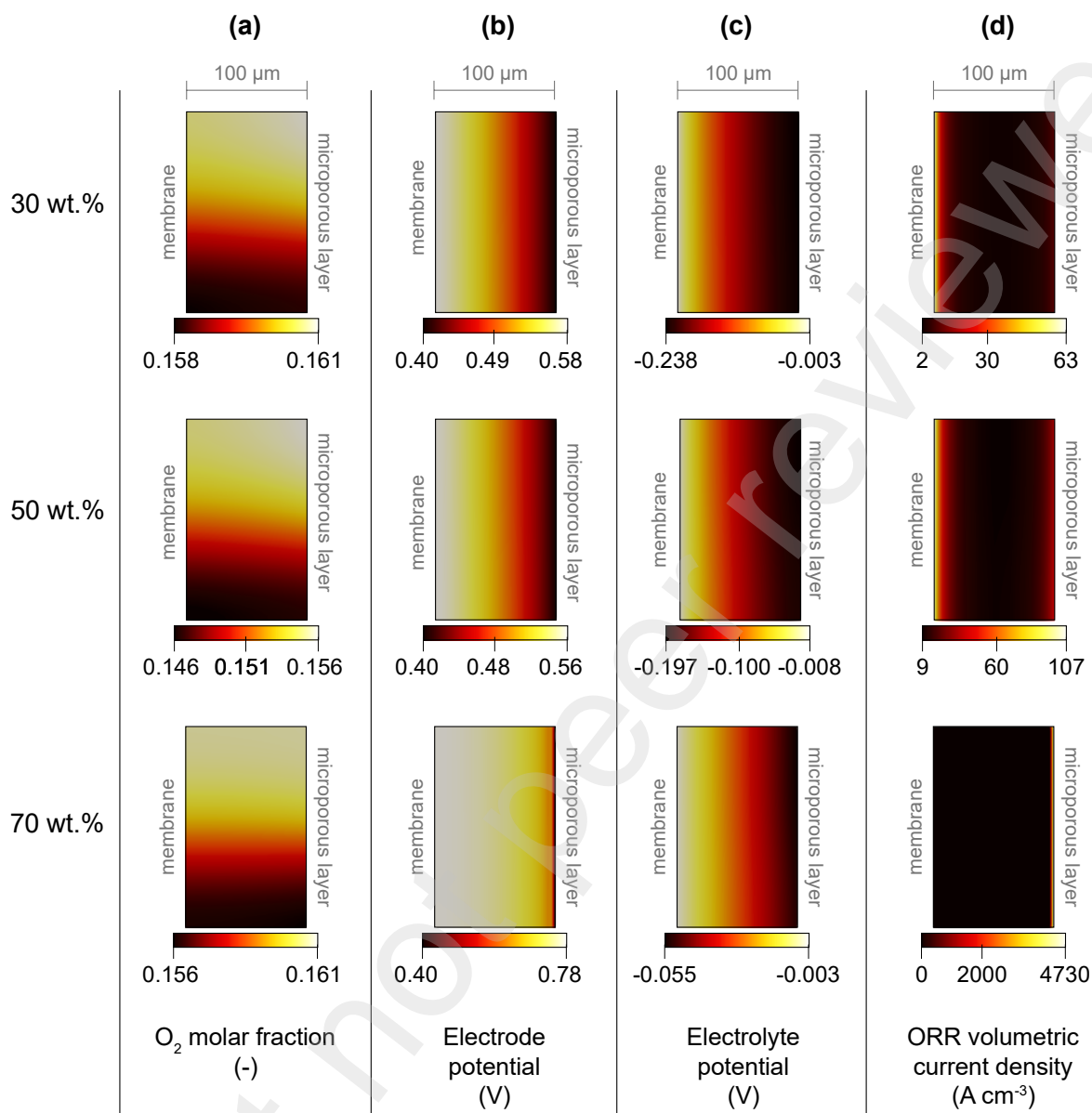


Figure 4 Two-dimensional distribution plots of O_2 mole fraction, electrode & electrolyte potentials, and cathodic volumetric current density for the non-PGM cathode catalyst layers with different ionomer loadings at $E_{cell} = 0.4\ V$: (a) 30 wt.%; (b) 50 wt.%; (c) 70 wt.%. Note: contour plots not drawn to scale.

The non-PGM electrode with 50 wt.% ionomer loading was used as the base case throughout the study. All simulations were executed at $RH = 70\%$ unless stated otherwise with air-fed cathode to simulate the practical operating conditions for commercial PEMFCs.

4.2. Effect of the reference exchange current density on the current distribution within the catalyst layer

The activity of non-PGM electrocatalyst has drastically increased in the past decade. Non-PGM catalysts can now compete with widely used Pt/C catalysts in terms of activity reported to the geometric surface, although they require far higher loadings (i.e., 4 mg cm^{-2} vs. $0.1 \text{ mg}_{\text{Pt}} \text{ cm}^{-2}$). This improvement arises from several directions, but the notable improvement is in the intrinsic activity of these materials, namely the reference exchange current density. To this end, we investigated the effect of i_0^{ref} on the current density at $E_{cell} = 0.9 \text{ V}$ (Figure 5a). The target activity of non-PGM catalysts specified by the US DOE is $\geq 0.044 \text{ A cm}^{-2}$ at $E_{cell} = 0.9 \text{ V}$ [58]. Figure 5a shows that the current density at 0.9 V increases with increasing i_0^{ref} as expected. Our simulation shows when i_0^{ref} is increased by 4 orders of magnitude (i.e., from 6.0×10^{-13} to $8.3 \times 10^{-9} \text{ A cm}^{-2}$), the target activity at 0.9 V was met. We also plotted the reaction distribution at different i_0^{ref} to see how the non-PGM layer is utilized (Figure 5b-d) at three different i_0^{ref} used in this parametric study. With the base case parameter (Figure 5b; $i_0^{ref} = 6 \times 10^{-13} \text{ A cm}^{-2}$), the volumetric current density at 0.9 V is close to zero everywhere in the layer due to low i_0^{ref} . As i_0^{ref} was increased by 4 orders of magnitude (Figure 5d; $6 \times 10^{-9} \text{ A cm}^{-2}$), the non-PGM layer is utilized more throughout the thickness. For all cases of i_0^{ref} , the reaction is concentrated near the membrane|cathode interface and the majority of the non-PGM layer is less utilized. This effect is more pronounced with high i_0^{ref} where the reaction hot spot is narrower compared to the cases with lower i_0^{ref} and the rest of the non-PGM layer is underutilized. This is attributed to the thickness of the non-PGM catalyst layer.

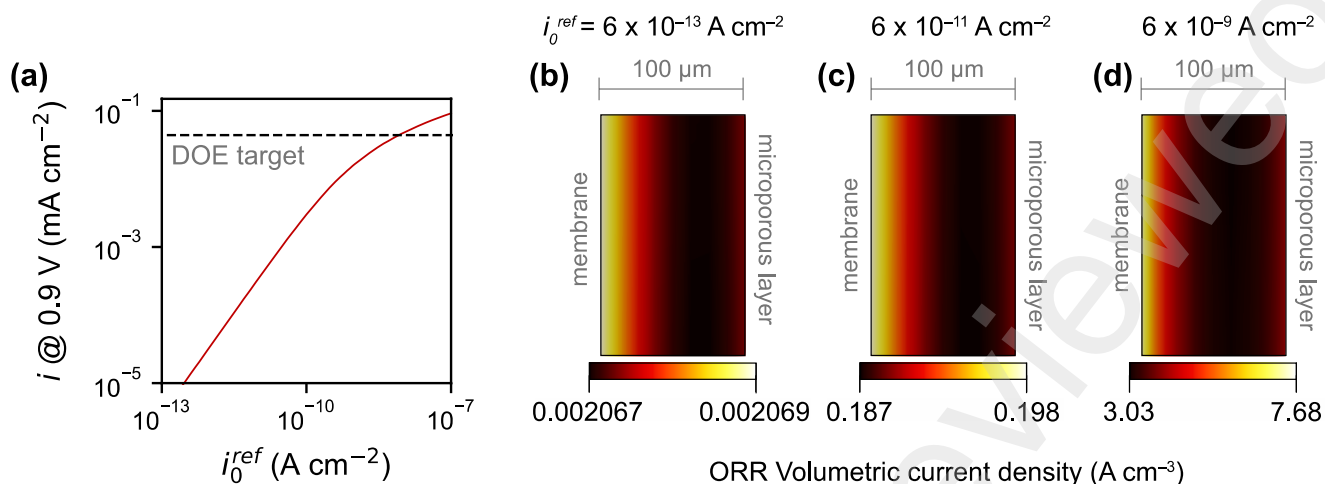


Figure 5 Parametric study on the reference exchange current density: (a) shows current densities at $E_{cell} = 0.9$ V with various reference exchange current densities. Two-dimensional reaction distribution is plotted for the non-PGM catalyst layers at (b) $i_0^{ref} = 6 \times 10^{-13}$ A cm $^{-2}$, (c) $i_0^{ref} = 6 \times 10^{-11}$ A cm $^{-2}$, and (d) $i_0^{ref} = 6 \times 10^{-9}$ A cm $^{-2}$

Practical fuel cells operate at cell voltages between 0.6 and 0.7 V. Electrocatalysis Consortium (ElectroCat) periodically releases their progress on non-PGM catalyst/catalyst layer development along with their interim target performance for non-PGM electrodes. In year 2021, their interim performance target for non-PGM electrode was ≥ 500 mA cm $^{-2}$ at $E_{cell} = 0.675$ V [59]. We therefore examined whether the current state of the catalytic activity (i.e., $i_0^{ref} = 6 \times 10^{-9}$ A cm $^{-2}$) was sufficient to meet this interim target (Figure 6). We highlight that the limiting process at 0.675 V are different thus, despite achieving the DOE activity target at $E_{cell} = 0.9$ V, the given electrocatalyst did not achieve the ElectroCat target at $E_{cell} = 0.675$ V. This is most likely due to large ohmic losses caused by low solid and electrolyte phase volume fractions as it was previously discussed. All these facts highlight that optimizing the catalyst layer structure is a requirement, in combination with increasing the intrinsic activity, to meet the performance targets proposed for the non-PGM electrodes.

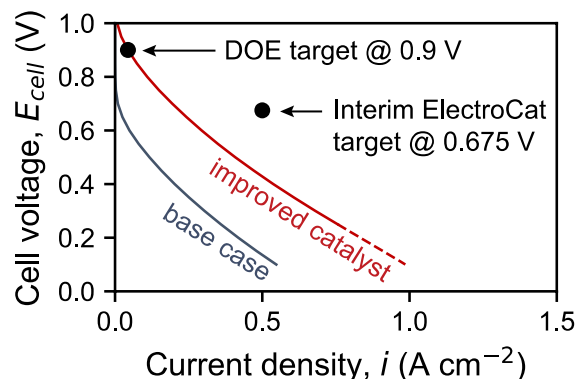


Figure 6 Predicted polarization curves for the base case (blue) and improved case where the catalytic activity (i.e., $i_0^{ref} = 6 \times 10^{-9} \text{ A cm}^{-2}$) is improved to meet the DOE target (red). By improving the catalytic activity, the DOE target is met at $E_{cell} = 0.9 \text{ V}$. However, catalyst layer optimization is still required to meet the target at $E_{cell} = 0.675 \text{ V}$.

4.3. Optimization of the non-PGM catalyst layer by tuning the thickness and porosity

Our assessment shows that the large electrode thickness and, in our case, the ultra-high porosity are the limiting factors in the non-PGM catalyst layer design. This is true independent of their i_0^{ref} . We owe this to the largely underutilized volume (Figure 5b-d) and the strong ohmic losses of the non-PGM electrodes. There are two ways to reduce the thickness of the non-PGM catalyst layers: 1) use lower catalyst mass loading; or 2) reduce the thickness of the non-PGM catalyst layer while keeping the catalyst mass loading the same. We initially explored the first approach. Lower catalyst mass loading will lead to lower catalyst layer thickness while the three phase volume fractions are kept the same (i.e., solid, electrolyte, and void). The volumetric catalyst loading was also kept the same. We have simulated non-PGM electrodes with varying mass loadings from 0.5 to 4 mg cm^{-2} , using $i_0^{ref} = 6 \times 10^{-13} \text{ A cm}^{-2}$ (Figure S1). We assumed that the thickness of the non-PGM electrode increased linearly by $33.3 \text{ }\mu\text{m}$ per 1 mg cm^{-2} of catalysts added (based on experimentally observing a thickness of $100 \text{ }\mu\text{m}$ with 3 mg cm^{-2}

catalyst loading [33]). Of note is that higher catalyst loading increases the performance at low current density (i.e., $E_{cell} = 0.9$ V). However, at higher current densities, higher catalyst loading shows an adverse effect on the performance because charge and mass transport are hindered by the thicker layer. A similar behavior was observed in other studies where higher current density was achieved with lower catalyst loading, but lower catalyst loading also yielded higher kinetic losses [25,60]. For $i_0^{ref} = 6 \times 10^{-13}$ A cm^{-2} , the optimal loading appears to be 3 mg cm^{-2} (Figure S1), as the model showed further increase in the mass loading diminishes the performance at higher current densities with only a minor kinetic benefit. This optimal catalyst loading coincides with many reported optimal catalyst loadings for non-PGM catalysts [17,25,60]. Some works have suggested higher catalyst loadings (e.g., $3 - 5 \text{ mg cm}^{-2}$) [26]. However, the picture drastically changes when considering higher i_0^{ref} . We gathered insights on this point by using the aforementioned i_0^{ref} and optimizing the catalyst loading for each of them at $E_{cell} = 0.675$ V (Figure 7). When i_0^{ref} was increased from 6×10^{-13} to 6×10^{-11} A cm^{-2} , a substantial improvement in the current density was observed at $E_{cell} = 0.675$ V over the entire range of catalyst mass loading. However, the target at $E_{cell} = 0.675$ V (i.e., 500 mA cm^{-2}) is not achieved. The optimal loading with $i_0^{ref} = 6 \times 10^{-11}$ A cm^{-2} is much lower (i.e., $m_{cat} = 0.54 \text{ mg cm}^{-2}$) indicating as the activity is increased, the performance of the non-PGM electrode becomes more charge/mass transport limited. At an $i_0^{ref} = 8.3 \times 10^{-9}$ A cm^{-2} , the performance target can be met by simply tuning the catalyst loading. Figure 7 shows that the mass loading of 1 mg cm^{-2} and below is sufficient.

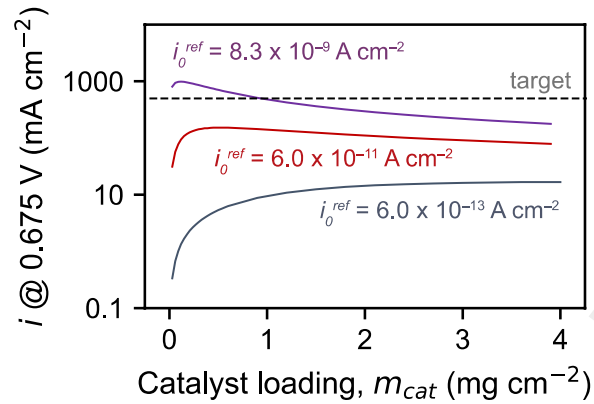


Figure 7 Optimal catalyst loading at three different reference exchange current densities: $6 \times 10^{-13} \text{ A cm}^{-2}$ (base case); $6 \times 10^{-11} \text{ A cm}^{-2}$ (moderate improvement); $8.3 \times 10^{-9} \text{ A cm}^{-2}$ (optimistic case)

The parametric study on the catalyst loading showed that depositing catalysts beyond a certain loading had adverse impact on the fuel cell performance due to increased transport resistances caused by the thicker layer. We therefore sought a way to mitigate this trade-off between catalyst loading and transport resistances by exploring the second approach. The second approach involves reducing the thickness of the electrode at a fixed catalyst mass loading. This approach offers a couple of benefits: 1) improved kinetics due to higher volumetric catalyst loading and specific surface area; and 2) reduced charge transfer resistances due to increased solid and electrolyte phase volume fraction. Reduced thickness can also improve the mass transport losses; however, a porosity reduction also needs to be considered with the decreasing thickness. We have recently shown that the thickness of the non-PGM catalyst layers can be modulated to a certain degree using the electrospraying technique [33]. Porous layers in PEMFCs can also undergo reduction in thicknesses due to compression during the cell assembly [61]. To test the effect of reduced thickness at a fixed catalyst mass loading, we varied the thickness of the non-PGM electrode from 100 μm to 30 μm at a fixed catalyst loading of 3 mg cm^{-2} (Figure 8) with $i_o^{ref} = 6 \times 10^{-13} \text{ A cm}^{-2}$ and 100- μm as the base case study. The volumetric catalyst loading, and the specific surface area were also

changed accordingly (Eq. (A.11)).

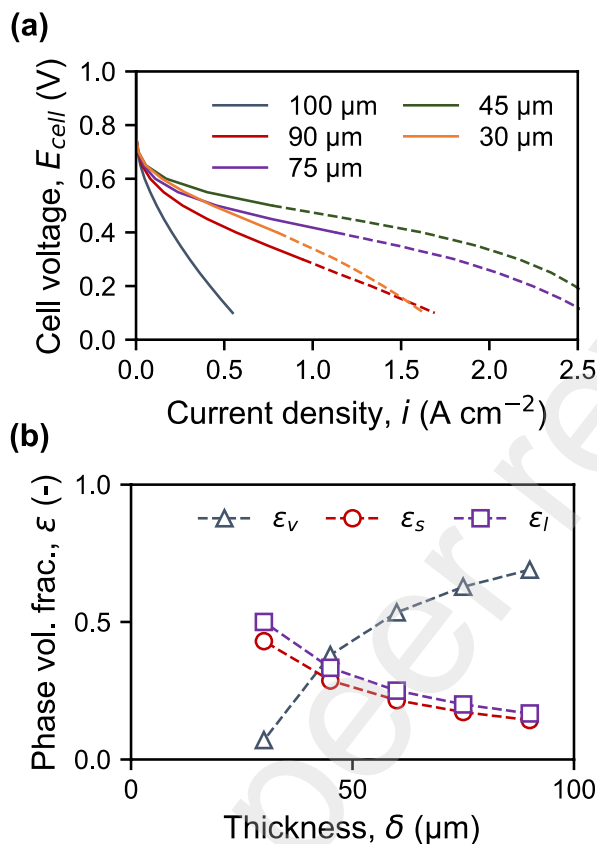


Figure 8 (a) Predicted polarization curves with different thicknesses at a fixed catalyst mass loading. (b) Void (ϵ_v), solid (ϵ_s), and electrolyte (ϵ_l) phase volume fractions at different thicknesses. The performance of the non-PGM electrodes improve by reducing the thickness to 45 μm . Further reduction in the thickness has adverse impact on the performance due to low porosity.

Decreasing the thickness of the non-PGM electrode from 100 μm to 45 μm resulted in a substantial performance improvement in the entire range of current densities (Figure 8a). This improvement is attributed to the increase in solid and electrolyte phase volume fractions (Figure 8b). When the thickness was further reduced to 30 μm , however, the current densities decreased over the entire range of the cell voltage. This reduction in the performance is attributed to the low porosity of the 30- μm electrode, which resulted O_2 depletion in the catalyst layer, as illustrated in Figure S2, as opposed to larger thicknesses.

Our analysis shows that the optimal phase composition for the non-PGM cathode catalyst layer is $\{\varepsilon_v, \varepsilon_s, \varepsilon_l\} = \{0.380, 0.287, 0.333\}$. The optimal porosity for the non-PGM cathode catalyst layer in this study is lower than the reported values elsewhere [33,36]. This led us to believe that the limiting factor for the performance of non-PGM electrodes is not necessarily a gas transport resistance, but the low electric and the low proton conductivity. We also add that, at low RH, the chance of electrode flooding is diminished which is another mass transport issue that frequently occurs with non-PGM electrodes operated with fully humidified air (or O₂). The latter point is discussed in more depth in the later part of this manuscript.

Based on the findings from the previous section, we can now assess how catalyst layers with various i_0^{ref} would fare with an optimized thickness and porosity ($m_{cat} = 3.0 \text{ mg cm}^{-2}$, $\{\varepsilon_v, \varepsilon_s, \varepsilon_l\} = \{0.380, 0.287, 0.333\}$). At $i_0^{ref} = 6 \times 10^{-13} \text{ A cm}^{-2}$, the simulation predicts that the ElectroCat interim target cannot be achieved (Figure 9a). Figure 9b shows that the interim target at 500 mA cm^{-2} can be met with $i_0^{ref} = 6.0 \times 10^{-11} \text{ A cm}^{-2}$. However, at this i_0^{ref} , the requirement at 0.9 V is not fulfilled (44 mA cm^{-2}).

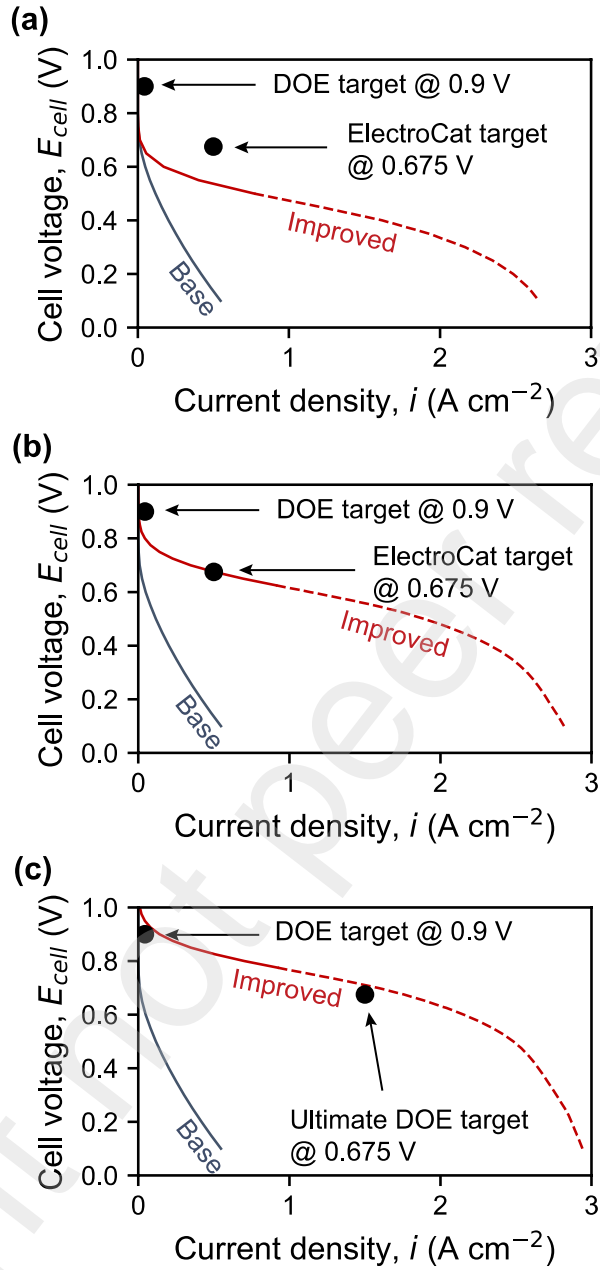


Figure 9 Predicted polarization curve for optimized non-PGM electrode structure at (a) $i_0^{ref} = 6 \times 10^{-13} \text{ A cm}^{-2}$; (b) $i_0^{ref} = 6 \times 10^{-11} \text{ A cm}^{-2}$; (c) $i_0^{ref} = 8.3 \times 10^{-9} \text{ A cm}^{-2}$

Finally, we sought to find out how much improvement in the fuel cell performance can be achieved

when the catalytic activity reaches its target performance (i.e., $i_0^{ref} = 8.3 \times 10^{-9} \text{ A cm}^{-2}$) with the optimized phase composition (i.e., $\{\varepsilon_v, \varepsilon_s, \varepsilon_l\} = \{0.380, 0.287, 0.333\}$ and thickness = 45 μm). Figure 9c shows that, with high catalytic activity and optimized electrode phase composition, both the US DOE catalytic activity target at 0.9 V and the ultimate fuel cell target (1.5 A cm^{-2} at 0.675 V) can be achieved even at low RH operation [59,62]. Note that the dotted lines in Figure 9 represents the non-physical region where $\text{RH} > 100\%$. Therefore, we can expect lower current densities in this region caused by mass transport loss due to liquid water condensation. Multiphase effect on the thick non-PGM electrodes require further study, nonetheless, our simulation results show that the structure and the composition of the non-PGM electrodes can be optimized to give the performance comparable to that of platinum-based electrodes given that the activity of the catalyst is sufficiently high, as it is currently becoming [18].

4.4. Water flooding under low RH operation

Besides the catalyst stability and durability issues [63], many studies have identified the water flooding as one of the main reasons for low performance of non-PGM electrodes [19,35,36,64]. However, these studies feed fully humidified air at the cathode to maximize the proton conductivity of the non-PGM electrodes. Therefore, we sought to investigate whether the electrode flooding was still a critical issue when non-PGM electrodes were operated at low RH. We first simulated polarization curves at two different RH (e.g., 70 and 90%) with the base case parameters (Figure 10a; $m_{cat} = 3 \text{ mg cm}^{-2}$, $\{\varepsilon_v, \varepsilon_s, \varepsilon_l\} = \{0.721, 0.129, 0.150\}$, and thickness = 100 μm).

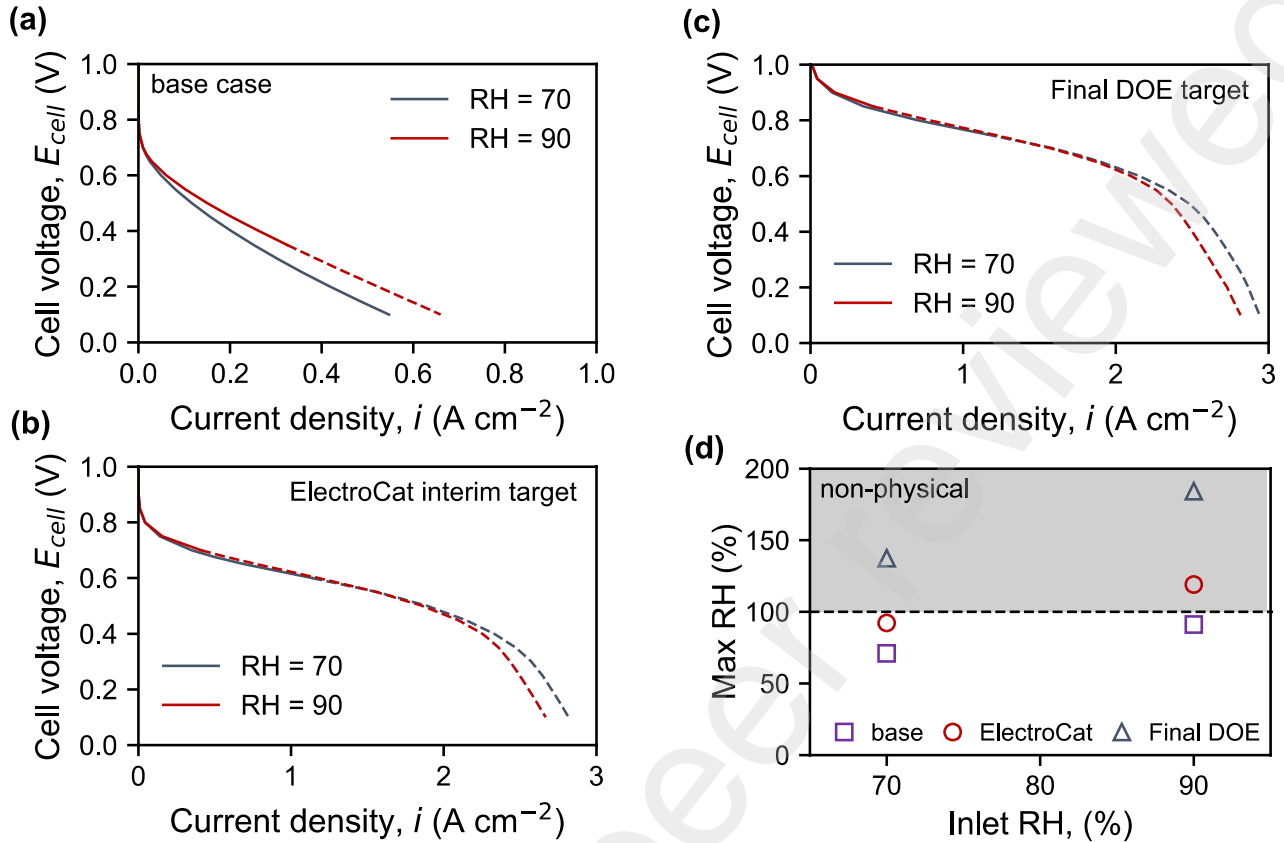


Figure 10 Multiphase behavior in non-PGM electrodes at different inlet RH (70, 90%): (a) predicted polarization curves with the based case parameter; $i_0^{ref} = 6 \times 10^{-13} A\ cm^{-2}$, $m_{cat} = 3\ mg\ cm^{-2}$, $\{\varepsilon_v, \varepsilon_s, \varepsilon_l\} = \{0.721, 0.129, 0.150\}$; (b) $i_0^{ref} = 6 \times 10^{-11} A\ cm^{-2}$, $m_{cat} = 3\ mg\ cm^{-2}$, $\{\varepsilon_v, \varepsilon_s, \varepsilon_l\} = \{0.380, 0.287, 0.333\}$; (c) $i_0^{ref} = 8.3 \times 10^{-9} A\ cm^{-2}$, $m_{cat} = 3\ mg\ cm^{-2}$, $\{\varepsilon_v, \varepsilon_s, \varepsilon_l\} = \{0.380, 0.287, 0.333\}$; (d) the maximum relative humidity for the three different scenarios (a, b, c) at $E_{cell} = 0.675$ V over the range of inlet RH. Dotted lines in (a), (b), (c) represent the region where $RH_{max} > 100\%$. In (d), $RH_{max} > 100\%$ is a non-physical region where water vapor is expected to condense into liquid water. RH_{max} was allowed to go above 100% due to single-phase assumption.

Figure 10a shows that, at lower inlet RH (e.g., $RH_{inlet} = 70\%$), the maximum RH (RH_{max}) within the MEA was $<100\%$ meaning that water vapor is not likely to condense into liquid water and flood the electrode pores provided the air stoichiometry is sufficiently high. For $RH_{inlet} = 90\%$, RH increased above 100% only below $E_{cell} < 0.5$ V. We then used $i_0^{ref} = 6.0 \times 10^{-11} A\ cm^{-2}$, along with optimal structural parameters, and an optimized thickness ($m_{cat} = 3\ mg\ cm^{-2}$) and porosity (phase composition $\{\varepsilon_v, \varepsilon_s, \varepsilon_l\}$)

= {0.380, 0.287, 0.333}), to examine whether the non-PGM electrodes are prone to water flooding at this stage (Figure 10b). RH_{\max} were generally higher due to more water produced at the cathode. For the inlet $RH = 70\%$, however, RH_{\max} only goes beyond 100% at $E_{cell} < 0.6$ V. Finally, we investigated whether water flooding would be a critical issue when the final DOE target has been met (e.g., at $i_{\text{ref}}^{\text{ref}} = 8.3 \times 10^{-9} \text{ A cm}^{-2}$), thus showing that the non-PGM electrode will likely suffer from water flooding even at low RH operation. To make this point clearer, we plotted RH_{\max} of three different scenarios against a range of RH_{inlet} at $E_{cell} = 0.675$ V in Figure 10d. The simulation predicts that under low RH operating conditions, the non-PGM electrodes are less prone to water flooding until the final DOE target is reached. We acknowledge the limitation of our continuum assumption and that we neglect the structural heterogeneity of the non-PGM electrode morphology observed by others [65]. For instance, some water vapor may condense into micro-/mesopores due to the Kelvin effect (i.e., the vapor pressure depression) and reconfigure itself to wet certain regions of the non-PGM electrode (e.g., membrane|catalyst layer interface) as pointed out in some studies [34,35,64].

5. Conclusion

In this study, we provide insights on designing non-PGM electrodes that are operated at low RH using an open-source finite element fuel cell simulation package, openFCST. In most studies, non-PGM electrodes are tested with fully humidified O₂/air. High RH may be beneficial for the proton conductivity and the short-term operation, but high RH operation is not desirable in the long term due to issues related to catalyst degradation and water flooding. We set out to explore whether low RH operation could provide feasible performance and explored options for improvement. The model was calibrated to experimental data by fitting the reference exchange current density and the effective electrical conductivity. Our model suggests that the electron transfer is hindered at high ionomer loading (e.g., > 50 wt.%). We attribute this behavior to the excess ionomer separating catalyst particles thus reducing the number of potential percolation pathways for the electrons.

Our simulation results indicate that high porosity (e.g., $\epsilon_v > 0.5$) may not necessarily be advantageous for designing non-PGM electrodes at low RH. In fact, our analysis showed that the high porosity was one of the main reasons why non-PGM performs poorly. Some works have shown that the higher porosity mitigates electrode flooding, however, at low RH, we have shown that the water flooding is less likely to occur, hence lower porosity is acceptable. Lower porosity has an added benefit of reducing the charge transport resistances. This is counter-intuitive to the conventional pursuit of higher porosity to counteract the much thicker CL. In fact, high solid and electrolyte phase volume fraction were shown to be the key to boosting the performance of the non-PGM electrodes. Our strategy to increase the solid and the ionomer volume fraction in this work, was to decrease the thickness of the non-PGM electrodes while keeping the catalyst loading consistent. This strategy has a couple of benefits: 1) improved kinetics by increased volumetric catalyst loading and the specific surface area; 2) enhanced ohmic resistances by increased solid

and electrolyte phase volume fraction and shorted transport lengths. This strategy can be realized by several approaches: 1) we have shown previously that the thickness of the non-PGM electrodes can be controlled to a certain degree at a fixed catalyst loading; 2) controlling the thickness of the non-PGM electrodes through controlled compression during cell assembly; 3) pre-compressing the non-PGM electrodes before the cell assembly; and 4) synthesizing non-PGM catalysts with smaller particle sizes to reduce the porosity and the thickness. Approach 4 can also help increasing the specific surface area of the non-PGM electrode.

Our simulation results show that the improvement in the non-PGM catalytic activity alone is not sufficient for the integration of non-PGM electrode in fuel cells, but it must be accompanied by the structure, composition, and transport optimization of the non-PGM electrode. Furthermore, our results also indicate that the optimization of the catalytic layer is dependent of the intrinsic activity of non-PGM electrocatalyst, along with its capability to operate without flooding.

Acknowledgement

The authors would like to express their gratitude to the Natural Science and Engineering Research Council (NSERC) of Canada for their financial support. This work was also partially funded by the Automotive Fuel Cell Company (AFCC) and Ballard Power Systems, Inc.

Nomenclature

Roman letters

a_w	Water activity, (-)
A_0	Catalyst surface area per unit mass of the catalyst particle, ($\text{cm}^2 \text{g}^{-1}$)
A_v	Area utilized for the oxygen reduction reaction per unit volume of catalyst layer, ($\text{cm}^2 \text{cm}^{-3}$)
c_i	Concentration of species i , (mol cm^{-3})
$D_{i,j}$	Fikian diffusion coefficient of species i and j , ($\text{cm}^2 \text{s}^{-1}$)
D_{ik}	Knudsen diffusion coefficient of species i , ($\text{cm}^2 \text{s}^{-1}$)
D_T	Thermo-osmotic diffusion coefficient, ($\text{g cm}^{-1} \text{s}^{-1} \text{K}^{-1}$)
E^{th}	Thermodynamic potential, (V)
EW	Membrane equivalent weight, (g mol^{-1})
f_{rxn}	fraction of reversible heat released in reaction rxn , (-)
F	Faraday's constant, (C mol^{-1})
ΔG_{rxn}°	Standard Gibbs free energy change in reaction, (J mol^{-1})
\bar{H}_i	Molar enthalpy of i , (J mol^{-1})
\bar{H}_{lv}	Molar latent heat of vaporization of water, (J mol^{-1})
\bar{H}_{sorp}	Molar enthalpy of sorption of water, (J mol^{-1})
$H_{i,N}$	Henry's constant for species i in Nafion®, ($\text{Pa cm}^3 \text{mol}^{-1}$)
i	Volumetric current density, (A cm^{-3})
i_0^{ref}	Reference exchange current density, (A cm^{-2})
j_{0T}	Exchange current density for Tafel-Volmer pathway in the dual-pathway

	kinetic model for hydrogen oxidation reaction, ($A\text{ cm}^{-2}$)
j_{0H}	Exchange current density for Heyrovsky-Volmer pathway in the dual-pathway kinetic model for hydrogen oxidation reaction, ($A\text{ cm}^{-2}$)
k	Thermal conductivity, ($W\text{ cm}^{-1}\text{ K}^{-1}$)
k_t	Rate constant for adsorption/desorption of water vapor in ionomer, (s^{-1})
L	Thickness
m_{pt}	Platinum mass loading, ($mg\text{ cm}^{-2}$)
M	Heat barrier resistance coefficient, (-)
M_i	Molecular weight of species i , ($g\text{ mol}^{-1}$)
n	Number of electrons transferred, (-) or Number of agglomerates per unit volume, (μm^{-3})
n_d	Electro-osmotic drag coefficient, (-)
p	Pressure, (Pa)
R	Gas constant, ($J\text{ mol}^{-1}\text{ K}^{-1}$)
RH	Relative humidity, (-)
S	Source
$\Delta\bar{S}_r$	Change in entropy per mole of fuel for reaction r , ($J\text{ mol}^{-1}\text{ K}^{-1}$)
ΔS_{rxn}°	Standard entropy change of reaction, ($J\text{ mol}^{-1}\text{ K}^{-1}$)
T	Temperature, (K)
V_{FeNC}	Fe-N/C volumetric loading, ($mg\text{ cm}^{-3}$)
V_m	Acid equivalent volume of membrane, EW/ρ_l , ($\text{cm}^3\text{ mol}^{-1}$)
x_i	Mole fraction of species i , (-)
x_i°	Mole fraction of i in the channel, (-)
y_i	Weight fraction of species i , (-)

Greek letters

α	Transfer coefficient, (-)
γ	Reaction order, (-)
ε_i	Volume fraction of phase i , (-)
ε_i^{th}	Percolation threshold of phase i , (-)
η	Overpotential, (V)
λ	Water content in electrolyte phase, (-)
λ_{eq}	Equilibrium water content in electrolyte phase, (-)
μ	Percolation network constant, (-)
ρ	Density, (g cm ⁻³)
σ_i	Conductivity ($i = s$ or l), (S cm ⁻¹)
ϕ_i	Potential ($i = s$ or l), (V)
ϕ_L	Thiele's modulus, (-)

Superscripts and subscripts

0 or <i>ref</i>	Reference property
<i>a</i>	Anode
<i>acl</i>	Anode catalyst layer
<i>c</i>	Cathode or Carbon
<i>ccl</i>	Cathode catalyst layer
<i>cl</i>	Catalyst layer
<i>eff</i>	Effective transport parameter
<i>FeNC</i>	Non-PGM or Fe-N/C catalyst
<i>HOR</i>	Hydrogen oxidation reaction
<i>ip</i>	In-plane
<i>l</i>	Electrolyte/ionomer
<i>N</i>	Nafion®
<i>ORR</i>	Oxygen reduction reaction
<i>overall</i>	Overall reaction
<i>pt</i>	Platinum
<i>s</i>	Solid
<i>tp</i>	Through-plane
<i>tot</i>	Total property of a gas mixture
<i>v</i>	Void
<i>w</i>	Water vapor

Preprint not peer reviewed

Appendix

A. Model parameters

A.1. Structural parameters

The solid and electrolyte phase volume fractions of the platinum-based anode catalyst layer was calculated by:

$$\varepsilon_s = \frac{m_{pt}}{L_{acl}} \left(\frac{1}{\rho_{pt}} + \frac{1 - y_{pt}}{y_{pt} \rho_c} \right) \quad (\text{A.1})$$

$$\varepsilon_l = \frac{m_{pt} y_l}{L_{acl} (1 - y_l) y_{pt} \rho_l} \quad (\text{A.2})$$

The solid and electrolyte phase volume fractions of the non-PGM cathode catalyst layer was calculated by:

$$\varepsilon_s = \frac{m_{FeNC}}{L_{ccl}} \frac{1}{\rho_{FeNC}} \quad (\text{A.3})$$

$$\varepsilon_l = \frac{m_{FeNC} y_l}{L_{ccl} (1 - y_l) \rho_l} \quad (\text{A.4})$$

The porosities for both catalyst layers were calculated by:

$$\varepsilon_v = 1 - \varepsilon_s - \varepsilon_l \quad (\text{A.5})$$

A.2. Electrochemical parameters

The thermodynamic cell potential is calculated by the Nernst equation [45]:

$$E^{th} = -\frac{\Delta G_{rxn}^\circ}{nF} + \frac{\Delta S_{rxn}^\circ}{nF} (T - T_0) + \frac{RT}{nF} \ln \left[\left(\frac{p_{H_2}}{p_0} \right) \left(\frac{p_{O_2}}{p_0} \right)^{1/2} \right] \quad (\text{A.6})$$

ΔG_{rxn}° and ΔS_{rxn}° are -237 kJ mol^{-1} and $-163 \text{ J mol}^{-1} \text{ K}^{-1}$, respectively, at standard temperature and pressure (e.g., $T_0 = 25^\circ\text{C}$ and $p_0 = 1.5 \text{ bar}$), assuming liquid water formation [45]. At $T = 80^\circ\text{C}$ and $p_{tot} = 1.5 \text{ bar}$ for both H_2 and air, E^{th} is approximately 1.2 V.

The volumetric current density of the cathode was determined using the Tafel equation [54]:

$$i = A_v i_0^{ref} \left(\frac{c_{O_2}^{naf}}{c_{O_2}^{ref}} \right)^\gamma e^{\alpha F \eta / RT} \quad (\text{A.7})$$

The concentration of oxygen dissolved in thin ionomer film at the active site ($c_{O_2}^{naf}$) is given by:

$$c_{O_2}^{naf} = \frac{c_t x_{O_2}}{H_{O_2,N}} \quad (\text{A.8})$$

The dimensionless Henry's law constant, $H_{O_2,N}$ is obtained by:

$$H_{O_2,N} = \frac{\hat{H}_{O_2,N}}{RT} \quad (\text{A.9})$$

$\hat{H}_{O_2,N}$ is taken to be $3.53 \times 10^4 \text{ Pa} \cdot \text{m}^3 \text{ mol}^{-1}$ [66].

The dual-path kinetics model proposed by Wang et al. [46] was used to determine the volumetric current density of the anode:

$$i = A_v \left(\frac{c_{H_2}}{c_{H_2}^{ref}} \right)^\gamma \left[j_{0T} (1 - e^{-2F\eta/\gamma RT}) + j_{0H} (e^{F\eta/2RT} - e^{-F\eta/\gamma RT} e^{-F\eta/2RT}) \right] \quad (\text{A.10})$$

The volumetric specific active surface area of the cathode catalyst layer, A_v , was calculated by assuming the entire catalyst surface was available for reaction:

$$A_v = A_0 \cdot V_{FeNC} = A_0 \frac{m_{FeNC}}{L_{ccl}} \quad (\text{A.11})$$

A_0 was measured by the gas sorption experiment (Quantachrome Gemini VII, US) using the BET equation.

A_0 was measured to be $650 \text{ m}^2 \text{ g}^{-1}$ [33].

A.3. Gaseous species transport parameters

The bulk diffusion coefficients in porous layers were calculated using the Bosanquet approximation ($1/D_i = 1/D_{ij} + 1/D_{ik}$) [33]. The molecular diffusivity (D_{ij}) was calculated by the Chapman-Enskog equation [49]. For MPLs and CLs, the Knudsen diffusivity (D_{ik}) was accounted for [33]. For MPLs, the Knudsen radius (r_k) of 56 nm was used. This value was calculated by the correlation obtained by Sabharwal et al. [67]:

$$r_k = r_p(1.66\varepsilon_v^{1.65} + 0.289) \quad (\text{A.12})$$

The primary particle radius of 39.5 nm was used for carbon black [52]. For non-PGM catalyst layers, $r_k = 300$ nm was used. This value was obtained experimentally by mercury intrusion porosimetry [33].

The effective diffusion coefficients (D_i^{eff}) in porous layers were calculated using various correlations. The Tomadakis-Sotirchos equation [68] was used for GDLs in both directions (in-plane & through-plane):

$$D_i^{eff} = D_i \varepsilon_v \left(\frac{\varepsilon_v - \varepsilon_v^{th}}{1 - \varepsilon_v^{th}} \right)^{\mu_v} H(\varepsilon_v - \varepsilon_v^{th}) \quad (\text{A.13})$$

The percolation equation was used to calculate D_i^{eff} of MPLs and CLs:

$$D_i^{eff} = D_i \left(\frac{\varepsilon_v - \varepsilon_v^{th}}{1 - \varepsilon_v^{th}} \right)^{\mu_v} H(\varepsilon_v - \varepsilon_v^{th}) \quad (\text{A.14})$$

Input parameters (i.e., ε_v^{th} and μ_v) for GDLs, MPLs, and CLs are given in Table B.2 and Table B.4

A.4. Charged species transport parameters

The effective electrical conductivities of all catalyst layers were determined by the percolation theory.

$$\sigma_s^{eff} = \sigma_s \left(\frac{\varepsilon_s - \varepsilon_s^{th}}{1 - \varepsilon_s^{th}} \right)^{\mu_s} H(\varepsilon_s - \varepsilon_s^{th}) \quad (\text{A.15})$$

Input parameters (i.e., ε_s^{th} , and μ_s) for CLs are given in Table B.2 and Table B.4. The effective electrical conductivities of GDLs and MPLs are given by the manufacturer and provided in Table B.2 and Table B.4.

In this study, we assumed that thin ionomer layers in catalyst layers and bulk ionomer have different proton conductivities. The effective proton conductivities in CLs were calculated by the third order polynomial expression obtained by fitting the experimental data provided by Iden et al. [69].

$$\sigma_l^{eff} = \varepsilon_l^{1.6} (1.931 \times 10^{-7} a_w^3 - 6.735 \times 10^{-6} a_w^2 + 0.00075 a_w - 0.008) \exp \left[751.5412 \left(\frac{1}{353} - \right) \right] \quad (\text{A.16})$$

where water activity, a_w is given by:

$$a_w = 100 \times \begin{cases} 0.000094\lambda^3 - 0.00865\lambda^2 + 0.1832\lambda - 0.1254, & \text{if } \lambda < 13 \\ 1, & \text{else} \end{cases} \quad (\text{A.17})$$

The bulk proton conductivity of Nafion[®] NRE-211 was calculated by the following expression. The expression was obtained by fitting a polynomial [70] through experimental data [71]:

$$\sigma_{l,bulk} = (-1.0125 \times 10^{-4} \lambda^2 + 0.01052\lambda - 0.020634) \exp \left[\frac{6248}{R} \left(\frac{1}{303} - \frac{1}{T} \right) \right] \quad (\text{A.18})$$

A.5. Sorbed water transport parameters

We adopted Springer's linear law for the electro-osmotic drag coefficient [72]:

$$n_d = \frac{2.5\lambda}{22} \quad (\text{A.19})$$

Motupally et al. [73] measured the water flux across the Nafion[®] 115 and obtained the following expression for water diffusivity in the ionomer, D_λ :

$$D_{\lambda} = \begin{cases} 3.10 \times 10^{-3} \lambda (-1 + e^{0.28\lambda}) \exp\left(-\frac{2436}{T}\right), & 0 < \lambda \leq 3 \\ 4.17 \times 10^{-3} \lambda (1 + 161e^{-\lambda}) \exp\left(-\frac{2436}{T}\right), & 3 < \lambda \leq 17 \end{cases} \quad (\text{A.20})$$

Kim and Mench [74] measured the thermo-osmotic fluxes on various ion exchange membranes including Nafion® membranes. They report the following Arrhenius-like expression for the thermo-osmotic diffusion coefficient, D_T , of Nafion® 112:

$$D_T = -1.04 \times 10^{-5} \exp\left(-\frac{2362}{T}\right) \quad (\text{A.21})$$

D_{λ} and D_T were adjusted for porosity and tortuosity effect by the following expression:

$$D_i^{eff} = D_i \varepsilon_i^{1.6} \quad (\text{A.22})$$

The equilibrium water content was determined by the expression [75]:

$$\lambda_{eq} = \left[1 + 0.2352RH^2 \left(\frac{T - 303}{30} \right) \right] (14.22RH^3 - 18.92RH^2 + 13.41RH) \quad (\text{A.23})$$

The water vapor pressure in relative humidity (RH) is [72]:

$$\log_{10}(p_{vap}) = -2.1794 + 0.02953\hat{T} - 9.1837 \times 10^{-5}\hat{T}^2 + 1.4454 \times 10^{-7}\hat{T}^3 \quad (\text{A.24})$$

A.6. Thermal transport parameters

The effective thermal conductivity of GDL in the through-plane direction is given by [76]:

$$k_{tp}^{eff} = M(-7.166 \times 10^{-6}\hat{T} + 2.24 \times 10^{-3}\hat{T}^2 - 0.237\hat{T} + 20.1) \quad (\text{A.25})$$

where M is the heat barrier resistance coefficient obtained by fitting the experimental data reported by Zamel et al. [76]:

$$M = -1.495 \times 10^{-11} \hat{T}^5 + 2.601 \times 10^{-9} \hat{T}^4 - 6.116 \times 10^{-8} \hat{T}^3 - 9.829 \times 10^{-6} \hat{T}^2 + 0.0664 \quad (\text{A.26})$$

The effective thermal conductivity of GDL in the through-plane direction is given by [77]:

$$k_{ip}^{eff} = -7.166 \times 10^{-6} \hat{T}^3 + 2.24 \times 10^{-3} \hat{T}^2 - 0.237 \hat{T} + 20.1 \quad (\text{A.27})$$

B. Input parameters

Table B.2, Table B.3, and Table B.4 summarizes input parameters used for the base case in this study

(Note: Manu. – specified by the manufacturer, Meas. – measured).

Table B.1 Base case geometric dimensions and operating conditions of the membrane electrode assembly

Parameter / unit	Value	Ref.
<i>Geometric properties</i>		
$L_{gdl} / \mu\text{m}$	190	Manu.
$L_{mpl} / \mu\text{m}$	45	Manu.
$L_{mem} / \mu\text{m}$	25	Manu.
$L_{acl} / \mu\text{m}$	2.5	[52]
$L_{ccl} / \mu\text{m}$	100	Meas.
Land width / cm	1	[44]
Channel width / cm	1	[44]
<i>Operating condition</i>		
$T_{cell} / ^\circ\text{C}$	80	This work
p / Pa	15000	This work
RH / %	70	This work

Table B.2 Physical and electrochemical properties of anode porous layers

Parameter / unit	Value	Ref.
------------------	-------	------

Constants

$\rho_{pt} / \text{g cm}^{-3}$	21.5	[53]
$\rho_c / \text{g cm}^{-3}$	2.0	[53]
$\rho_l / \text{g cm}^{-3}$	2.0	[53]

Transport properties

$D_{H_2,w} / \text{cm}^2 \text{s}^{-1}$	0.801	[49]
$H_{H_2,n} / \text{Pa cm}^3 \text{mol}^{-1}$	6.69×10^{10}	[78]
$D_{H_2,n} / \text{cm}^2 \text{s}^{-1}$	12.8×10^{-6}	[78]
$\sigma_{s,tp}^{eff,gdl} / \text{S cm}^{-1}$	4	Manu.
$\sigma_{s,ip}^{eff,gdl} / \text{S cm}^{-1}$	180	Manu.
$\sigma_{s}^{eff,mpl} / \text{S cm}^{-1}$	0.823	Manu.
$\sigma_{s,c} / \text{S cm}^{-1}$	88.84	[44]
$\varepsilon_{v,tp}^{th,gdl} / -$	0.11	[79]
$\mu_{v,tp}^{gdl} / -$	3.479	[79]
$\varepsilon_{v,ip}^{th,gdl} / -$	0.11	[80]
$\mu_{v,ip}^{gdl} / -$	2.576	[80]
$\varepsilon_v^{th,mpl} / -$	0.118	[43]
$\mu_v^{mpl} / -$	2	[43]
$\varepsilon_v^{th,acl} / -$	0.25884	[43]
$\mu_v^{acl} / -$	2	[43]
$\varepsilon_s^{th,acl} / -$	0.1	[43]
$\mu_s^{acl} / -$	2	[43]

Structural properties

$\varepsilon_v^{gdl} / -$	0.8	Manu.
$\varepsilon_v^{mpl} / -$	0.4	Manu.
$m_{pt} / \text{mg cm}^{-2}$	0.1	This work

Pt C / -	0.46	This work
----------	------	-----------

Electrochemical parameters (dual-pathway)

$j_{OT} / \text{A cm}^{-2}$	0.47	[46]
$j_{OH} / \text{A cm}^{-2}$	0.01	[46]
$\gamma / -$	1.2	[46]
$c_{H_2}^{ref} / \text{mol cm}^{-3}$	0.59	[78]

Table B.3 Physical and electrochemical properties of the membrane/ionomer

Parameter / unit	Value	Ref.
<i>Membrane properties</i>		
$EW / \text{g cm}^{-3}$	1100	[72]
$\rho_{l,dry} / \text{g cm}^{-3}$	2.0	[72]
k / s^{-1}	10000	This work

Table B.4 Physical and electrochemical properties of cathode porous layers

Parameter / unit	Value	Ref.
<i>Constants</i>		
$\rho_{FeNC} / \text{g cm}^{-3}$	2.326	Meas.
$\rho_l / \text{g cm}^{-3}$	2.0	[53]
<i>Transport properties</i>		
$D_{O_2,N_2} / \text{cm}^2 \text{s}^{-1}$	0.187	[49]
$D_{w,N_2} / \text{cm}^2 \text{s}^{-1}$	0.233	[49]
$H_{O_2,n} / \text{Pa cm}^3 \text{mol}^{-1}$	3.17×10^{10}	[78]
$D_{O_2,n} / \text{cm}^2 \text{s}^{-1}$	8.45×10^{-6}	[78]
$\sigma_{s,tp}^{eff,gdl} / \text{S cm}^{-1}$	4	Manu.

$\sigma_{s,ip}^{eff,gdl} / S cm^{-1}$	180	Manu.
$\sigma_{s}^{eff,mpl} / S cm^{-1}$	0.823	Manu.
$\sigma_{s,c} / S cm^{-1}$	88.84	[44]
$\varepsilon_{v,tp}^{th,gdl} / -$	0.11	[79]
$\mu_{v,tp}^{gdl} / -$	3.479	[79]
$\varepsilon_{v,ip}^{th,gdl} / -$	0.11	[80]
$\mu_{v,ip}^{gdl} / -$	2.576	[80]
$\varepsilon_{v}^{th,mpl} / -$	0.118	[43]
$\mu_{v}^{mpl} / -$	2	[43]
$\varepsilon_{v}^{th,ccl} / -$	0	[33]
$\mu_{v}^{ccl} / -$	2.716	[33]
$\varepsilon_{s}^{th,ccl} / -$	0.118	This work
$\mu_{s}^{ccl} / -$	2.13	This work

Structural properties

$\varepsilon_{v}^{gdl} / -$	0.8	Manu.
$\varepsilon_{v}^{mpl} / -$	0.4	Manu.
$m_{FeNC} / mg cm^{-2}$	3	This work

Electrochemical parameters (Tafel kinetics)

$\alpha / -$	1	[55]
$n / -$	4	[55]
$\gamma / -$	0.5	[55]
$i_0^{ref} / \mu A cm^{-2}$	6×10^{-7}	This work
$c_{O_2}^{ref} / mol cm^{-3}$	0.59	[55]

References

- [1] R.L. Borup, A. Kusoglu, K.C. Neyerlin, R. Mukundan, R.K. Ahluwalia, D.A. Cullen, K.L. More, A.Z. Weber, D.J. Myers, Recent developments in catalyst-related PEM fuel cell durability, *Curr. Opin. Electrochem.* 21 (2020) 192–200. <https://doi.org/10.1016/j.coelec.2020.02.007>.
- [2] D.A. Cullen, K.C. Neyerlin, R.K. Ahluwalia, R. Mukundan, K.L. More, R.L. Borup, A.Z. Weber, D.J. Myers, A. Kusoglu, New roads and challenges for fuel cells in heavy-duty transportation, *Nat. Energy.* (2021). <https://doi.org/10.1038/s41560-021-00775-z>.
- [3] S. Shukla, K. Domican, K. Karan, S. Bhattacharjee, M. Secanell, Analysis of Low Platinum Loading Thin Polymer Electrolyte Fuel Cell Electrodes Prepared by Inkjet Printing, *Electrochimica Acta.* 156 (2015) 289–300. <https://doi.org/10.1016/j.electacta.2015.01.028>.
- [4] S. Shukla, D. Stanier, M.S. Saha, J. Stumper, M. Secanell, Analysis of Inkjet Printed PEFC Electrodes with Varying Platinum Loading, *J. Electrochem. Soc.* 163 (2016) F677–F687. <https://doi.org/10.1149/2.1111607jes>.
- [5] A. Orfanidi, P. Madkikar, H.A. El-Sayed, G.S. Harzer, T. Kratky, H.A. Gasteiger, The Key to High Performance Low Pt Loaded Electrodes, *J. Electrochem. Soc.* 164 (2017) F418–F426. <https://doi.org/10.1149/2.1621704jes>.
- [6] V. Yarlagaadda, M.K. Carpenter, T.E. Moylan, R.S. Kukreja, R. Koestner, W. Gu, L. Thompson, A. Kongkanand, Boosting Fuel Cell Performance with Accessible Carbon Mesopores, *ACS Energy Lett.* 3 (2018) 618–621. <https://doi.org/10.1021/acsenerylett.8b00186>.
- [7] J.J. Conde, M.A. Folgado, P. Ferreira-Aparicio, A.M. Chaparro, A. Chowdhury, A. Kusoglu, D. Cullen, A.Z. Weber, Mass-transport properties of electrosprayed Pt/C catalyst layers for polymer-electrolyte fuel cells, *J. Power Sources.* 427 (2019) 250–259. <https://doi.org/10.1016/j.jpowsour.2019.04.079>.
- [8] A. Sánchez-Ramos, J.T. Gostick, P.A. García-Salaberri, Modeling the Effect of Low Pt loading Cathode Catalyst Layer in Polymer Electrolyte Fuel Cells: Part I. Model Formulation and Validation, *J. Electrochem. Soc.* 168 (2021) 124514. <https://doi.org/10.1149/1945-7111/ac4456>.
- [9] D.-H. Lee, G.-T. Yun, G. Doo, S. Yuk, H. Guim, Y. Kim, W.-B. Jung, H.-T. Jung, H.-T. Kim, Hierarchical Wrinkle-Structured Catalyst Layer/Membrane Interface for Ultralow Pt-Loading Polymer Electrolyte Membrane Fuel Cells (PEMFCs), *Nano Lett.* (2022). <https://doi.org/10.1021/acs.nanolett.1c04354>.
- [10] S.T. Thompson, B.D. James, J.M. Huya-Kouadio, C. Houchins, D.A. DeSantis, R. Ahluwalia, A.R. Wilson, G. Kleen, D. Papageorgopoulos, Direct hydrogen fuel cell electric vehicle cost analysis: System and high-volume manufacturing description, validation, and outlook, *J. Power Sources.* 399 (2018) 304–313. <https://doi.org/10.1016/j.jpowsour.2018.07.100>.
- [11] S.T. Thompson, D. Papageorgopoulos, Platinum group metal-free catalysts boost cost competitiveness of fuel cell vehicles, *Nat. Catal.* 2 (2019) 558–561. <https://doi.org/10.1038/s41929-019-0291-x>.
- [12] E. Proietti, F. Jaouen, M. Lefèvre, N. Larouche, J. Tian, J. Herranz, J.-P. Dodelet, Iron-based cathode catalyst with enhanced power density in polymer electrolyte membrane fuel cells, *Nat. Commun.* 2 (2011) 416. <https://doi.org/10.1038/ncomms1427>.
- [13] J. Shui, C. Chen, L. Grabstanowicz, D. Zhao, D.-J. Liu, Highly efficient nonprecious metal catalyst prepared with metal–organic framework in a continuous carbon nanofibrous network, *Proc. Natl. Acad. Sci.* 112 (2015) 10629–10634. <https://doi.org/10.1073/pnas.1507159112>.

- [14] H.T. Chung, D.A. Cullen, D. Higgins, B.T. Sneed, E.F. Holby, K.L. More, P. Zelenay, Direct atomic-level insight into the active sites of a high-performance PGM-free ORR catalyst, *Science*. 357 (2017) 479–484. <https://doi.org/10.1126/science.aan2255>.
- [15] X. Wan, X. Liu, Y. Li, R. Yu, L. Zheng, W. Yan, H. Wang, M. Xu, J. Shui, Fe–N–C electrocatalyst with dense active sites and efficient mass transport for high-performance proton exchange membrane fuel cells, *Nat. Catal.* 2 (2019) 259–268. <https://doi.org/10.1038/s41929-019-0237-3>.
- [16] H. Zhang, H.T. Chung, D.A. Cullen, S. Wagner, U.I. Kramm, K.L. More, P. Zelenay, G. Wu, High-performance fuel cell cathodes exclusively containing atomically dispersed iron active sites, *Energy Environ. Sci.* 12 (2019) 2548–2558. <https://doi.org/10.1039/C9EE00877B>.
- [17] A. Uddin, L. Dunsmore, H. Zhang, L. Hu, G. Wu, S. Litster, High Power Density Platinum Group Metal-free Cathodes for Polymer Electrolyte Fuel Cells, *ACS Appl. Mater. Interfaces*. 12 (2020) 2216–2224. <https://doi.org/10.1021/acsami.9b13945>.
- [18] S. Liu, C. Li, M.J. Zachman, Y. Zeng, H. Yu, B. Li, M. Wang, J. Braaten, J. Liu, H.M. Meyer, M. Lucero, A.J. Kropf, E.E. Alp, Q. Gong, Q. Shi, Z. Feng, H. Xu, G. Wang, D.J. Myers, J. Xie, D.A. Cullen, S. Litster, G. Wu, Atomically dispersed iron sites with a nitrogen–carbon coating as highly active and durable oxygen reduction catalysts for fuel cells, *Nat. Energy*. 7 (2022) 652–663. <https://doi.org/10.1038/s41560-022-01062-1>.
- [19] S.K. Babu, H.T. Chung, P. Zelenay, S. Litster, Modeling Electrochemical Performance of the Hierarchical Morphology of Precious Group Metal-Free Cathode for Polymer Electrolyte Fuel Cell, *J. Electrochem. Soc.* 164 (2017) F1037–F1049. <https://doi.org/10.1149/2.0041712jes>.
- [20] F. Jaouen, D. Jones, N. Coutard, V. Artero, P. Strasser, A. Kucernak, Toward Platinum Group Metal-Free Catalysts for Hydrogen/Air Proton-Exchange Membrane Fuel Cells, *Johns. Matthey Technol. Rev.* 62 (2018) 231–255. <https://doi.org/10.1595/205651318X696828>.
- [21] D. Banham, S. Ye, Current Status and Future Development of Catalyst Materials and Catalyst Layers for Proton Exchange Membrane Fuel Cells: An Industrial Perspective, *ACS Energy Lett.* 2 (2017) 629–638. <https://doi.org/10.1021/acsenergylett.6b00644>.
- [22] D. Banham, J.-Y. Choi, T. Kishimoto, S. Ye, Integrating PGM-Free Catalysts into Catalyst Layers and Proton Exchange Membrane Fuel Cell Devices, *Adv. Mater.* (2019) 1804846. <https://doi.org/10.1002/adma.201804846>.
- [23] L. Osmieri, Q. Meyer, Recent advances in integrating platinum group metal-free catalysts in proton exchange membrane fuel cells, *Curr. Opin. Electrochem.* 31 (2022) 100847. <https://doi.org/10.1016/j.coelec.2021.100847>.
- [24] D. Bokach, S. ten Hoopen, N. Muthuswamy, M.E.M. Buan, M. Rønning, Nitrogen-doped carbon nanofiber catalyst for ORR in PEM fuel cell stack: Performance, durability and market application aspects, *Int. J. Hydrog. Energy*. 41 (2016) 17616–17630. <https://doi.org/10.1016/j.ijhydene.2016.07.137>.
- [25] D. Banham, T. Kishimoto, Y. Zhou, T. Sato, K. Bai, J. Ozaki, Y. Imashiro, S. Ye, Critical advancements in achieving high power and stable nonprecious metal catalyst-based MEAs for real-world proton exchange membrane fuel cell applications, *Sci. Adv.* 4 (2018) eaar7180. <https://doi.org/10.1126/sciadv.aar7180>.
- [26] L. Osmieri, H. Wang, K.C. Neyerlin, Impact of Fabrication and Testing Parameters on the Performance of a Polymer Electrolyte Fuel Cell with Platinum Group Metal (PGM)-Free Cathode Catalyst, *J. Electrochem. Soc.* 168 (2021) 014503. <https://doi.org/10.1149/1945-7111/abd48e>.
- [27] X. Yin, H.T. Chung, S.K. Babu, U. Martinez, G.M. Purdy, P. Zelenay, Effects of MEA Fabrication

- and Ionomer Composition on Fuel Cell Performance of PGM-Free ORR Catalyst, *ECS Trans.* 77 (2017) 1273–1281. <https://doi.org/10.1149/07711.1273ecst>.
- [28] S. Komini Babu, H.T. Chung, P. Zelenay, S. Litster, Resolving Electrode Morphology's Impact on Platinum Group Metal-Free Cathode Performance Using Nano-CT of 3D Hierarchical Pore and Ionomer Distribution, *ACS Appl. Mater. Interfaces.* 8 (2016) 32764–32777. <https://doi.org/10.1021/acsami.6b08844>.
- [29] G. Wang, L. Osmieri, A.G. Star, J. Pfeilsticker, K.C. Neyerlin, Elucidating the Role of Ionomer in the Performance of Platinum Group Metal-free Catalyst Layer via in situ Electrochemical Diagnostics, *J. Electrochem. Soc.* 167 (2020) 044519. <https://doi.org/10.1149/1945-7111/ab7aa1>.
- [30] S. Khandavalli, R. Iyer, J.H. Park, D.J. Myers, K.C. Neyerlin, M. Ulsh, S.A. Mauger, Effect of Dispersion Medium Composition and Ionomer Concentration on the Microstructure and Rheology of Fe–N–C Platinum Group Metal-free Catalyst Inks for Polymer Electrolyte Membrane Fuel Cells, *Langmuir.* 36 (2020) 12247–12260. <https://doi.org/10.1021/acs.langmuir.0c02015>.
- [31] J. Li, S. Brüller, D.C. Sabarirajan, N. Ranjbar-Sahraie, M.T. Sougrati, S. Cavaliere, D. Jones, I.V. Zenyuk, A. Zitolo, F. Jaouen, Designing the 3D Architecture of PGM-Free Cathodes for H₂/Air Proton Exchange Membrane Fuel Cells, *ACS Appl. Energy Mater.* 2 (2019) 7211–7222. <https://doi.org/10.1021/acsaem.9b01181>.
- [32] S. Kabir, S. Medina, G. Wang, G. Bender, S. Pylypenko, K.C. Neyerlin, Improving the bulk gas transport of Fe-N-C platinum group metal-free nanofiber electrodes via electrospinning for fuel cell applications, *Nano Energy.* 73 (2020) 104791. <https://doi.org/10.1016/j.nanoen.2020.104791>.
- [33] Y. Kim, T. Asset, F. Wei, P. Atanassov, M. Secanell, J. Barralet, J.T. Gostick, Fabrication of platinum group metal-free catalyst layer with enhanced mass transport characteristics via an electrospaying technique, *Mater. Today Energy.* 20 (2021) 100641. <https://doi.org/10.1016/j.mtener.2021.100641>.
- [34] S.J. Normile, D.C. Sabarirajan, O. Calzada, V. De Andrade, X. Xiao, P. Mandal, D.Y. Parkinson, A. Serov, P. Atanassov, I.V. Zenyuk, Direct observations of liquid water formation at nano- and micro-scale in platinum group metal-free electrodes by operando X-ray computed tomography, *Mater. Today Energy.* 9 (2018) 187–197. <https://doi.org/10.1016/j.mtener.2018.05.011>.
- [35] J. Liu, M.R. Talarposhti, T. Asset, D.C. Sabarirajan, D.Y. Parkinson, P. Atanassov, I.V. Zenyuk, Understanding the Role of Interfaces for Water Management in Platinum Group Metal-Free Electrodes in Polymer Electrolyte Fuel Cells, *ACS Appl. Energy Mater.* 2 (2019) 3542–3553. <https://doi.org/10.1021/acsaem.9b00292>.
- [36] S. Komini Babu, D. Spornjak, R. Mukundan, D.S. Hussey, D.L. Jacobson, H.T. Chung, G. Wu, A.J. Steinbach, S. Litster, R.L. Borup, P. Zelenay, Understanding water management in platinum group metal-free electrodes using neutron imaging, *J. Power Sources.* 472 (2020) 228442. <https://doi.org/10.1016/j.jpowsour.2020.228442>.
- [37] E.C. Kumbur, M.M. Mench, FUEL CELLS – PROTON-EXCHANGE MEMBRANE FUEL CELLS | Water Management, in: J. Garche (Ed.), *Encycl. Electrochem. Power Sources*, Elsevier, Amsterdam, 2009: pp. 828–847. <https://doi.org/10.1016/B978-044452745-5.00862-5>.
- [38] F. Nandjou, J.-P. Poirot-Crouvezier, M. Chandesris, J.-F. Blachot, C. Bonnaud, Y. Bultel, Impact of heat and water management on proton exchange membrane fuel cells degradation in automotive application, *J. Power Sources.* 326 (2016) 182–192. <https://doi.org/10.1016/j.jpowsour.2016.07.004>.
- [39] H. Li, Y. Tang, Z. Wang, Z. Shi, S. Wu, D. Song, J. Zhang, K. Fatih, J. Zhang, H. Wang, Z. Liu, R. Abouatallah, A. Mazza, A review of water flooding issues in the proton exchange membrane fuel

- cell, *J. Power Sources*. 178 (2008) 103–117. <https://doi.org/10.1016/j.jpowsour.2007.12.068>.
- [40] A. Kusoglu, A.M. Karlsson, M.H. Santare, S. Cleghorn, W.B. Johnson, Mechanical behavior of fuel cell membranes under humidity cycles and effect of swelling anisotropy on the fatigue stresses, *J. Power Sources*. 170 (2007) 345–358. <https://doi.org/10.1016/j.jpowsour.2007.03.063>.
- [41] M.J. Workman, A. Serov, L. Tsui, P. Atanassov, K. Artyushkova, Fe–N–C Catalyst Graphitic Layer Structure and Fuel Cell Performance, *ACS Energy Lett.* 2 (2017) 1489–1493. <https://doi.org/10.1021/acsenergylett.7b00391>.
- [42] M.J. Workman, M. Dzara, C. Ngo, S. Pylypenko, A. Serov, S. McKinney, J. Gordon, P. Atanassov, K. Artyushkova, Platinum group metal-free electrocatalysts: Effects of synthesis on structure and performance in proton-exchange membrane fuel cell cathodes, *J. Power Sources*. 348 (2017) 30–39. <https://doi.org/10.1016/j.jpowsour.2017.02.067>.
- [43] M. Bhaiya, A. Putz, M. Secanell, Analysis of non-isothermal effects on polymer electrolyte fuel cell electrode assemblies, *Electrochimica Acta*. 147 (2014) 294–309. <https://doi.org/10.1016/j.electacta.2014.09.051>.
- [44] M. Secanell, R. Songprakorp, N. Djilali, A. Suleman, Optimization of a proton exchange membrane fuel cell membrane electrode assembly, *Struct. Multidiscip. Optim.* 40 (2010) 563–583. <https://doi.org/10.1007/s00158-009-0387-z>.
- [45] R. O’Hayre, S.-W. Cha, W.G. Corella, F.B. Prinz, *Fuel Cell Fundamentals*, 3rd ed., Wiley, n.d.
- [46] J.X. Wang, T.E. Springer, R.R. Adzic, Dual-Pathway Kinetic Equation for the Hydrogen Oxidation Reaction on Pt Electrodes, *J. Electrochem. Soc.* 153 (2006) A1732–A1740.
- [47] H. Wu, X. Li, P. Berg, On the modeling of water transport in polymer electrolyte membrane fuel cells, *Electrochimica Acta*. 54 (2009) 6913–6927. <https://doi.org/10.1016/j.electacta.2009.06.070>.
- [48] A.Z. Weber, R.L. Borup, R.M. Darling, P.K. Das, T.J. Dursch, W. Gu, D. Harvey, A. Kusoglu, S. Litster, M.M. Mench, R. Mukundan, J.P. Owejan, J.G. Pharoah, M. Secanell, I.V. Zenyuk, A Critical Review of Modeling Transport Phenomena in Polymer-Electrolyte Fuel Cells, *J. Electrochem. Soc.* 161 (2014) F1254–F1299. <https://doi.org/10.1149/2.0751412jes>.
- [49] Y. Kim, J.T. Gostick, Measuring effective diffusivity in porous media with a gasket-free, radial arrangement, *Int. J. Heat Mass Transf.* 129 (2019) 1023–1030. <https://doi.org/10.1016/j.ijheatmasstransfer.2018.10.054>.
- [50] M. Secanell, A. Putz, P. Wardlaw, V. Zingan, M. Bhaiya, M. Moore, J. Zhou, C. Balen, K. Domican, OpenFCST: An Open-Source Mathematical Modelling Software for Polymer Electrolyte Fuel Cells, *ECS Trans.* 64 (2014) 655–680. <https://doi.org/10.1149/06403.0655ecst>.
- [51] T.A. Davis, Algorithm 832: UMFPACK V4.3---an unsymmetric-pattern multifrontal method, *ACM Trans. Math. Softw.* 30 (2004) 196–199. <https://doi.org/10.1145/992200.992206>.
- [52] A. Kosakian, L.P. Urbina, A. Heaman, M. Secanell, Understanding single-phase water-management signatures in fuel-cell impedance spectra: A numerical study, *Electrochimica Acta*. 350 (2020) 136204. <https://doi.org/10.1016/j.electacta.2020.136204>.
- [53] D. Song, Q. Wang, Z. Liu, T. Navessin, M. Eikerling, S. Holdcroft, Numerical optimization study of the catalyst layer of PEM fuel cell cathode, *J. Power Sources*. 126 (2004) 104–111. <https://doi.org/10.1016/j.jpowsour.2003.08.043>.
- [54] M. Secanell, B. Carnes, A. Suleman, N. Djilali, Numerical optimization of proton exchange membrane fuel cell cathodes, *Electrochimica Acta*. 52 (2007) 2668–2682. <https://doi.org/10.1016/j.electacta.2006.09.049>.
- [55] A. Parthasarathy, Temperature Dependence of the Electrode Kinetics of Oxygen Reduction at the

- Platinum/Nafion® Interface—A Microelectrode Investigation, *J. Electrochem. Soc.* 139 (1992) 2530. <https://doi.org/10.1149/1.2221258>.
- [56] A.A. Kulikovskiy, J. Divisek, A.A. Kornyshev, Modeling the Cathode Compartment of Polymer Electrolyte Fuel Cells: Dead and Active Reaction Zones, *J. Electrochem. Soc.* 146 (1999) 3981. <https://doi.org/10.1149/1.1392580>.
- [57] K.C. Neyerlin, W. Gu, J. Jorne, H.A. Gasteiger, Determination of Catalyst Unique Parameters for the Oxygen Reduction Reaction in a PEMFC, *J. Electrochem. Soc.* 153 (2006) A1955. <https://doi.org/10.1149/1.2266294>.
- [58] DOE Technical Targets for Polymer Electrolyte Membrane Fuel Cell Components, (n.d.). <https://www.energy.gov/eere/fuelcells/doe-technical-targets-polymer-electrolyte-membrane-fuel-cell-components>.
- [59] P. Zelenay, L.A.N. Laboratory, ElectroCat 2.0 (Electrocatalysis Consortium), (n.d.) 54.
- [60] A. Baricci, A. Bisello, A. Serov, M. Odgaard, P. Atanassov, A. Casalegno, Analysis of the effect of catalyst layer thickness on the performance and durability of platinum group metal-free catalysts for polymer electrolyte membrane fuel cells, *Sustain. Energy Fuels*. 3 (2019) 3375–3386. <https://doi.org/10.1039/C9SE00252A>.
- [61] T.G. Tranter, J.T. Gostick, A.D. Burns, W.F. Gale, Pore Network Modeling of Compressed Fuel Cell Components with OpenPNM, *Fuel Cells*. 16 (2016) 504–515. <https://doi.org/10.1002/fuce.201500168>.
- [62] L. Osmieri, J. Park, D.A. Cullen, P. Zelenay, D.J. Myers, K.C. Neyerlin, Status and challenges for the application of platinum group metal-free catalysts in proton-exchange membrane fuel cells, *Curr. Opin. Electrochem.* 25 (2021) 100627. <https://doi.org/10.1016/j.coelec.2020.08.009>.
- [63] Y. He, G. Wu, PGM-Free Oxygen-Reduction Catalyst Development for Proton-Exchange Membrane Fuel Cells: Challenges, Solutions, and Promises, *Acc. Mater. Res.* (2022). <https://doi.org/10.1021/accountsmr.1c00226>.
- [64] P. Satjaritanun, I.V. Zenyuk, Water management strategies for PGM-free catalyst layers for polymer electrolyte fuel cells, *Curr. Opin. Electrochem.* 25 (2021) 100622. <https://doi.org/10.1016/j.coelec.2020.08.004>.
- [65] A. Serov, A.D. Shum, X. Xiao, V. De Andrade, K. Artyushkova, I.V. Zenyuk, P. Atanassov, Nano-structured platinum group metal-free catalysts and their integration in fuel cell electrode architectures, *Appl. Catal. B Environ.* 237 (2018) 1139–1147. <https://doi.org/10.1016/j.apcatb.2017.08.067>.
- [66] W. Sun, B.A. Peppley, K. Karan, An improved two-dimensional agglomerate cathode model to study the influence of catalyst layer structural parameters, *Electrochimica Acta*. 50 (2005) 3359–3374. <https://doi.org/10.1016/j.electacta.2004.12.009>.
- [67] M. Sabharwal, L.M. Pant, N. Patel, M. Secanell, Computational Analysis of Gas Transport in Fuel Cell Catalyst Layer under Dry and Partially Saturated Conditions, *J. Electrochem. Soc.* 166 (2019) F3065–F3080. <https://doi.org/10.1149/2.0081907jes>.
- [68] M.M. Tomadakis, S.V. Sotirchos, Ordinary, transition, and Knudsen regime diffusion in random capillary structures, *Chem. Eng. Sci.* 48 (1993) 3323–3333. [https://doi.org/10.1016/0009-2509\(93\)80149-K](https://doi.org/10.1016/0009-2509(93)80149-K).
- [69] H. Iden, K. Sato, A. Ohma, K. Shinohara, Relationship among Microstructure, Ionomer Property and Proton Transport in Pseudo Catalyst Layers, *J. Electrochem. Soc.* 158 (2011) B987–B994. <https://doi.org/10.1149/1.3598141>.
- [70] P. Dobson, C. Lei, T. Navessin, M. Secanell, Characterization of the PEM Fuel Cell Catalyst Layer

- Microstructure by Nonlinear Least-Squares Parameter Estimation, *J. Electrochem. Soc.* 159 (2012) B514–B523. <https://doi.org/10.1149/2.041205jes>.
- [71] J. Peron, A. Mani, X. Zhao, D. Edwards, M. Adachi, T. Soboleva, Z. Shi, Z. Xie, T. Navessin, S. Holdcroft, Properties of Nafion® NR-211 membranes for PEMFCs, *J. Membr. Sci.* 356 (2010) 44–51. <https://doi.org/10.1016/j.memsci.2010.03.025>.
- [72] T.E. Springer, Polymer Electrolyte Fuel Cell Model, *J. Electrochem. Soc.* 138 (1991) 2334. <https://doi.org/10.1149/1.2085971>.
- [73] S. Motupally, A.J. Becker, J.W. Weidner, Diffusion of Water in Nafion 115 Membranes, *J. Electrochem. Soc.* 147 (2000) 3171–3177. <https://doi.org/10.1149/1.1393879>.
- [74] S. Kim, M.M. Mench, Investigation of temperature-driven water transport in polymer electrolyte fuel cell: Thermo-osmosis in membranes, *J. Membr. Sci.* 328 (2009) 113–120. <https://doi.org/10.1016/j.memsci.2008.11.043>.
- [75] Y. Liu, M.W. Murphy, D.R. Baker, W. Gu, C. Ji, J. Jorne, H.A. Gasteiger, Proton Conduction and Oxygen Reduction Kinetics in PEM Fuel Cell Cathodes: Effects of Ionomer-to-Carbon Ratio and Relative Humidity, *J. Electrochem. Soc.* 156 (2009) B970. <https://doi.org/10.1149/1.3143965>.
- [76] N. Zamel, E. Litovsky, X. Li, J. Kleiman, Measurement of the through-plane thermal conductivity of carbon paper diffusion media for the temperature range from -50 to $+120^{\circ}\text{C}$, *Int. J. Hydrog. Energy.* 36 (2011) 12618–12625. <https://doi.org/10.1016/j.ijhydene.2011.06.097>.
- [77] N. Zamel, E. Litovsky, S. Shakhshir, X. Li, J. Kleiman, Measurement of in-plane thermal conductivity of carbon paper diffusion media in the temperature range of -20°C to $+120^{\circ}\text{C}$, *Appl. Energy.* 88 (2011) 3042–3050. <https://doi.org/10.1016/j.apenergy.2011.02.037>.
- [78] K. Karan, Assessment of transport-limited catalyst utilization for engineering of ultra-low Pt loading polymer electrolyte fuel cell anode, *Electrochem. Commun.* 9 (2007) 747–753. <https://doi.org/10.1016/j.elecom.2006.10.057>.
- [79] R. Flückiger, S.A. Freunberger, D. Kramer, A. Wokaun, G.G. Scherer, F.N. Büchi, Anisotropic, effective diffusivity of porous gas diffusion layer materials for PEFC, *Electrochimica Acta.* 54 (2008) 551–559. <https://doi.org/10.1016/j.electacta.2008.07.034>.
- [80] R.R. Rashapov, J.T. Gostick, In-Plane Effective Diffusivity in PEMFC Gas Diffusion Layers, *Transp. Porous Media.* 115 (2016) 411–433. <https://doi.org/10.1007/s11242-016-0648-4>.